Posted on 21 Nov 2022 — The copyright holder is the author/funder. All rights reserved. No reuse without permission. — https://doi.org/10.1002/essoar.10509513.1 — This a preprint and has not been peer reviewed. Data may be preliminary.

Thermolab: a thermodynamics laboratory for non-linear transport processes in open systems

Johannes Christiaan Vrijmoed[1] and Yuri Yurivech Podladchikov[2]

[1]Freie Universität Berlin
[2]University of Lausanne

November 21, 2022

Abstract

We developed a numerical thermodynamics laboratory called "Thermolab" to study the effects of the thermodynamic behavior of non-ideal solution models on reactive transport processes in open systems. The equations of state of internally consistent thermodynamic datasets are implemented in MATLAB functions and form the basis for calculating Gibbs energy. A linear algebraic approach is used in Thermolab to compute Gibbs energy of mixing for multi-component phases to study the impact of the non-ideality of solution models on transport processes. The Gibbs energies are benchmarked with experimental data, phase diagrams and other thermodynamic software. Constrained Gibbs minimization is exemplified with MATLAB codes and iterative refinement of composition of mixtures may be used to increase precision and accuracy. All needed transport variables such as densities, phase compositions, and chemical potentials are obtained from Gibbs energy of the stable phases after the minimization in Thermolab. We demonstrate the use of precomputed local equilibrium data obtained with Thermolab in reactive transport models. In reactive fluid flow the shape and the velocity of the reaction front vary depending on the non-linearity of the partitioning of a component in fluid and solid. We argue that non-ideality of solution models has to be taken into account and further explored in reactive transport models. Thermolab Gibbs energies can be used in Cahn-Hilliard models for non-linear diffusion and phase growth. This presents a transient process towards equilibrium and avoids computational problems arising during precomputing of equilibrium data.

Hosted file

`essoar.10509513.1.docx` available at https://authorea.com/users/526981/articles/596522-thermolab-a-thermodynamics-laboratory-for-non-linear-transport-processes-in-open-systems

Thermolab: a thermodynamics laboratory for non-linear transport processes in open systems

J. C. Vrijmoed[1], and Y. Y. Podladchikov[2]

[1]Institute of Geological Sciences, Freie Universität Berlin, Berlin, Germany.

[2]Institute of Earth Science, University of Lausanne, Lausanne, Switzerland.

Corresponding author: Johannes Vrijmoed (j.c.vrijmoed@fu-berlin.de)

Key Points:

- Thermolab: a set of MATLAB codes is presented to perform equilibrium and non-equilibrium thermodynamic calculations.
- Local thermodynamic equilibrium is used to study effects o non-ideality of solution models non-linear transport processes.
- Non-linear diffusion processes are investigated with Thermolab providing a transient natural physical process towards equilibrium.

Abstract

We developed a numerical thermodynamics laboratory called "Thermolab" to study the effects of the thermodynamic behavior of non-ideal solution models on reactive transport processes in open systems. The equations of state of internally consistent thermodynamic datasets are implemented in MATLAB functions and form the basis for calculating Gibbs energy. A linear algebraic approach is used in Thermolab to compute Gibbs energy of mixing for multi-component phases to study the impact of the non-ideality of solution models on transport processes. The Gibbs energies are benchmarked with experimental data, phase diagrams and other thermodynamic software. Constrained Gibbs minimization is exemplified with MATLAB codes and iterative refinement of composition of mixtures may be used to increase precision and accuracy. All needed transport variables such as densities, phase compositions, and chemical potentials are obtained from Gibbs energy of the stable phases after the minimization in Thermolab. We demonstrate the use of precomputed local equilibrium data obtained with Thermolab in reactive transport models. In reactive fluid flow the shape and the velocity of the reaction front vary depending on the non-linearity of the partitioning of a component in fluid and solid. We argue that non-ideality of solution models has to be taken into account and further explored in reactive transport models. Thermolab Gibbs energies can be used in Cahn-Hilliard models for non-linear diffusion and phase growth. This presents a transient process towards equilibrium and avoids computational problems arising during precomputing of equilibrium data.

Plain Language Summary

The behavior of Earth materials, rocks, minerals, melts, fluids and gases is important to predict physical processes in the Earth with computer models. The purpose of this is to study how the changes of variables such as fluid and solid composition influence the diffusion, fluid flow and reaction in rocks. Here we present a set of computer codes, called Thermolab, to calculate important physical properties such as density and chemical composition of solids, fluids and melts in chemical equilibrium. The calculations are based on the Gibbs energy that exists for every material. We use computer codes, written in MATLAB/OCTAVE language, to show how this Gibbs energy is calculated and used to compute chemical equilibrium and find the physical properties such as density, and chemical composition. We discuss techniques for accurate calculation of chemical equilibrium and physical properties in real rocks. Finally, we use Thermolab to formulate a computer model of fluids reacting with rocks. We find that chemical composition of the fluid and rock strongly affect the speed and shape of the boundary between reacted and unreacted rock. Thermolab can be used in phase growth models to investigate the way in which rocks develop towards equilibrium.

1 Introduction

One of the primary goals in Earth Science is to understand the physical processes that govern natural phenomena. This will facilitate prediction of potential hazardous events, such as earthquakes, volcanic eruptions, and related threats such as tsunamis (Fagents et al., 2013; Geller, 1997; Rundle et al., 2021; Ulrich et al., 2019). Predicting causes and effects of climate change, the reduction of global warming by storing CO_2, or the safety of storing nuclear waste, strongly rely on the understanding of underlying coupled physical processes (Orr, 2018; X. Zhang et al., 2022). Furthermore, the exploration of fossil fuels and raw materials in economic ore deposits, and most importantly the transition to renewable energy rely on a good understanding of the physics of geological processes (Feng et al., 2021; Vehling et al., 2020;

Weis et al., 2012). In many cases, numerical models that solve the mathematical equations governing the physics are the only way to predict such natural processes. Even though most coupled natural processes are non-equilibrium processes, the local equilibrium thermodynamic assumption is needed to close the system of mass, momentum, and energy equations and construct the model (De Groot & Mazur, 1984; Lebon et al., 2008). Without the knowledge of thermodynamic behavior of rocks, minerals, melts, fluids and gases involved in the process quantitative and predictive models cannot be constructed.

Transport processes such as diffusion, advection, and deformation, play a major role in all the important topics and are nearly always coupled to chemical reactions. Thus, reactive transport models have been a subject of geoscience research for many years (Steefel, 2019; Steefel et al., 2005). A large number of reactive transport codes has been developed particularly with the focus of subsurface processes (Kulik et al., 2012; Steefel et al., 2014), and applied to relevant geological problems in the subsurface (e. g. Sonnenthal et al., 2005; Wanner et al., 2014). A thorough review of the vast amount of work on reactive transport would be too extensive for the scope of this paper. For an overview of the main reactive transport codes in use for subsurface processes see Steefel et al. (2014).

Natural observations on, for example, exposed mantle rocks exhumed from great depth can be used to learn something about natural processes of CO_2 sequestration (Kelemen & Matter, 2008) and may lead to new insights for human carbon storage. In this context, knowledge of the thermodynamic behavior of minerals is also important for industrial processes and may lead to useful discoveries for example for carbon sequestration (Glasser et al., 2016).

Large scale geodynamic processes influence processes at the Earth's surface and play a role in the global geochemical cycles, the water budget, melt generation at ocean ridges and in collision zones, and erosion in mountain belts. In subduction zones these processes are closely interconnected as dehydration of hydrated oceanic lithosphere generates fluids that may trigger earthquakes and induce melting in the mantle wedge that may ultimately lead to volcanism at the surface, including direct effects on climate (Bebout et al., 2018). Numerical models have been useful in gaining more understanding of the physical processes of migration fluids from the subducting slab upwards (Wilson et al., 2014). Migration and melt focusing due to reaction infiltration instabilities have been studied by Aharonov et al. (1995). Connolly (1997) showed how coupling of dehydration reactions produce fluids that travel up in a visco-elastic matrix creating porosity waves as a mechanism for fluid migration. Balashov and Yardley (1998) investigated the effect of reaction on porosity structer and fluid pressure variation. More recent models further investigated fluid focusing, transport and reaction processes (Tian & Ague, 2014).

Recent progress in some of the important topics above has been made possible by coupling the local equilibrium thermodynamics to transport codes. Plümper et al. (2017) showed how the initialization of dehydration in subduction zones is dominated by chemical heterogeneities that control the thermodynamics on the micro-scale. Coupled to mass conservation and fluid flow, these local chemical heterogeneities lead from an initially formed local porosity to the development of fluid pathways.

The time scales of geological processes can vary between milliseconds to billion of years (Beinlich et al., 2020). With the use of numerical models combined with field observations, the duration of geological processes originally thought to be on the geological time scales have been

shown to be much faster (Ague & Baxter, 2007; Beinlich et al., 2020; John et al., 2012). Therefore, the prediction of the speed of reaction fronts, and elemental transport hinges on quantitative models obeying mass, momentum and energy conservation. Beinlich et al. (2020) used a reactive transport code coupled to local equilibrium thermodynamics to constrain the speed of natural CO_2 sequestration in serpentinites. The details behind the thermodynamic calculations in Beinlich et al. (2020) are given in this paper.

Nonideality of the solution models and its impact on the convexity of the flow functions (the so-called 'isotherms') has long been recognized as an important control on mass transport in porous reactive flows (Guy, 1993; Lichtner & Carey, 2006). However, it is underexplored mostly due to lack of transport models coupled to thermodynamically complex nonideal models including coupled substitutions, non-convex energy functions and ordering.

We present a numerical thermodynamics laboratory which we shall call "Thermolab", to do thermodynamic calculations on rocks, minerals, melts, and fluids involving aqueous species. We further show how this can be used in reactive transport models that are based on laws of mass, momentum, and energy conservation. Code examples are written in MATLAB/OCTAVE as it provides a transparent way of translating the mathematics and documenting the algorithms. Matlab also provides a prototype coding development platform. Short matlab codes serve as 'flow charts' used in the past to document the algorithms. The advantage of the MATLAB/OCTAVE codes compared to the 'flow charts' is that those are actually working computer programs, and can be copy-pasted from the figure and executed. Once working these codes can also be easily translated to any preferred programming language for optimization and supercomputing. The focus in this contribution is entirely on the technicalities with limited example applications. We document the nonideality of the models and the impact on non-linear transport processes in open systems by showing examples of how this can be achieved with Thermolab. Future studies will be investigating the impact of the nonideality on mass transport.

2 Background and motivation

A typical set of equations that governs the physics of the reactive transport based on Beinlich et al. (2020) is shown to motivate the use of equilibrium thermodynamics in transport processes. Total mass conservation in which Darcy flux is used:

$$\frac{\partial}{\partial t}\left(\rho_f\phi+\rho_s\left(1-\phi\right)\right)=\nabla\cdot\left(\rho_f\frac{k^0\phi^3}{\mu_f}\left(\nabla P_f+\rho_f g\right)\right) \tag{1}$$

Mass conservation of an immobile species in the solid:

$$\frac{\partial}{\partial t}\left(\rho_s C_{s_{im}}\left(1-\phi\right)\right)=0 \tag{2}$$

Mass concentration balance of a mobile species in the fluid:

$$\frac{\partial}{\partial t}\left(\rho_f\varphi C_f+\rho_f\left(1-\varphi\right)C_s\right)-\nabla\bullet\left(\rho_f C_f\frac{k^0\varphi^3}{\mu_f}\left(\nabla P_f+\rho_f g\right)\right)=\nabla\bullet\left(\rho_f\varphi C_f D_{C_f}\nabla\mu_{C_f}\right) \tag{3}$$

From this set of equations, we need to compute the local solid density, fluid density, chemical potential, mobile species concentration in fluid, and in solid, and one immobile species

concentration in solid. When the transport of material in the fluid is neglected, the third equation is omitted and the system reduces to the set of equations of Plümper et al. (2017). In any case, fluid and minerals have variable composition and density. This leaves a system of three equations for eight unknowns: fluid and solid density (ρ_f), and (ρ_s), weight fraction of a mobile component in fluid and solid (C_f), and (C_s), chemical composition of the component in the fluid (μ_{Cf}), and the weight fraction of an immobile component in the solid ($C_{s,im}$), porosity (ϕ), and fluid pressure (P_f). Background permeability (k^0), fluid viscosity (μ_f) and diffusion coefficient of mobile component C_f in the fluid (D_{Cf}) are given. Porosity, fluid pressure and either the fluid or the solid composition of each component in the system are not thermodynamically constrained and the three equations are solved for ϕ, P_f and C_s. The remaining unknown solid and fluid compositions and densities are found from thermodynamic relationships assuming local equilibrium at each point in time and in space in the model. In complex mineral, melt and fluid solutions, the non-ideal mixing behaviour leads to non-linear thermodynamic relationships. We compute these relationships with Thermolab, benchmarked with phase diagrams for rocks, fluids and melts. Using MATLAB codes, the first part of this contribution documents the technical details of the equilibrium thermodynamic calculations and the treatment of solid solutions. This is considered essential to understand the effects on non-linear transport processes. We include a description of methods to sufficiently resolve the equilibrium compositions and densities of the involved phases. This is needed to avoid numerical artefacts and instability in the transport codes. In the last part, we get back to the details of the implementation and solution of a system of transport equations in which all quantities evolve through time. For a full list of symbols and notation see Table 1.

Table 1 List of symbols and abbreviations. Symbols in italics for scalar variables, bold font for vectors, and bold capitals to denote matrices.

Symbol	Meaning	Units	MATLAB
ρ_f	Density of fluid	kg/m^3	**rhof**
ρ_s	Density of solid	kg/m^3	**rhos**
φ	Porosity (volume fraction of fluid)	volume fraction	**phi**
C_f	Concentration of component in fluid	weight fraction	**Cf**
C_s	Concentration of component in solid	weight fraction	**Cs**
k^0	background permeability	m^2	**k0**
μ_f	fluid viscosity	Pa s	**muf**
P_f	fluid pressure	Pa	**Pf**
t	time	s	**t**
g	gravitational acceleration	m/s^2	**grav**
D_{Cf}	diffusion coefficient of component in fluid	m^2/s	**DCf**
μ_{Cf}	Chemical potential of component in fluid	J/mol	**mu_Cf**
$C_{s,im}$	concentration of immobile component in solid	weight fraction	**Cs_im**
g^0	Specific endmember gibbs energy	J/mol	**G**
s^0	Specific endmember entropy	J/mol	**S**
h^0	Enthalpy	J/mol	**H**
T	Temperature	K	**T**
P	Pressure	kbar	**P**
R	Universal gas constant	J/mol/K	**R**
$g^0{}_r$	Specific endmember gibbs energy at 1 bar, 25 °C	J/mol	**Gr**
$s^0{}_r$	Entropy at reference conditions (1 bar, 25 °C)	J/mol	**Sr**
$h^0{}_r$	Enthalpy at reference conditions (1 bar, 25 °C)	J/mol	**Hr**
$v^0{}_r$	Volume at reference conditions (1 bar, 25 °C)	J/bar	**Vr**
a	heat capacity coefficient	kJ/K	**a**
b	heat capacity coefficient	kJ/K^2	**b**

c	heat capacity coefficient	kJ K	`c`
d	heat capacity coefficient	kJ $K^{-1/2}$	`d`
a_{MRK}	Fluid EOS coefficient	kJ^2 kbar $K^{1/2}$ mol^{-2}	`a`
b_{MRK}	Fluid EOS coefficient	kJ $kbar^{-1}$ mol^{-1}	`b`
K	bulk modulus	kbar	`k`
K'	derivative of bulk modulus	kbar	`kp`
c_P	Heat capacity	J/mol/K	`Cp`
ν	Stoiciometric coefficents in chemical reaction	mol	`v`
G_{sys}	Gibbs energy of system	J	`Gsys`
g_{mix}	Specific gibbs energy of a mixture	J/mol	`gmix`
g_{mech}	Specific gibbs energy of a mechanical mixing	J/mol	`gmech`
g_{id}	Specific gibbs energy of a ideal mixing	J/mol	`gid`
g_{nid}	Specific gibbs energy of a non-ideal mixing	J/mol	`gnid`
p	Vector of proportions of endmember in a mixture	mol fraction	`p`
m	Site multiplicity in ideal mixing energy	mol	`mtpl`
z	Vector of site fraction in a mixture	mol fraction	`z`
S_t	Site occupancy table	mol	`st`
Z_t	Site fraction endmember matrix	mol fraction	`zt`
K_{eq}	Equilibrium constant	-	`Keq`
ΔG^0_{rxn}	Difference in g^0 between products and reactants	J	`dGrxn`
α	Molar amount of phase from Gibbs minimization	mol	`alph`
$\mathbf{N_{phs}}$	Matrix of composition of phases in mol	mol	`Nphs`
$\mathbf{n_{sys}}$	Vector of system compositions in mol	mol	`nsys`
V_{mol}	Molar volume	m^3/mol	`Vmol`
$\mathbf{m_{mol}}$	Molar mass of phase vector	kg/mol	`Mmol`
molm	Molar mass of components vector	kg/mol	`molm`
ρ	Density of a phase	kg/m^3	`rho`
ϕ_p	Volume fraction of phase	-	`phi_p`
ϕ_{mol}	Mole fraction of phase	-	`phi_m`
ϕ_{wt}	Weight fraction of phase	-	`phi_wt`
$\boldsymbol{\rho_{ss}}$	Vector of densities of solids	kg/m^3	`rho(solid_id)`
$\boldsymbol{\phi_{ss}}$	Vector of volume fraction of solids	-	`phi_p(solid_id)`
ρ_{tot}	Total density	kg/m^3	`rho_t`
β_e	Effective compressibility	Pa^{-1}	`beta_e`
μ_1	Chemical potential of component 1	J/mol	`mu_1`
D_{Cs}	Diffusion coefficient in solid	m^2/s	`Dc_s`
γ	Cahn-Hilliard surface energy parameter	J/mol	`gam`

3 Gibbs energy calculation

The starting point of equilibrium thermodynamic calculations in Thermolab is the Gibbs energy of a mineral, melt, or fluid. All other required properties are derived from the Gibbs energy. The calculation of Gibbs energies requires in the first place an internally consistent thermodynamic dataset for pure solids, fluids, gases, or aqueous species, often referred to as endmembers. Secondly, it needs solution models that describe the energy of mixing between endmembers dissolved in a phase, also referred to as mixing models or activity-composition relationships (e.g. Ganguly, 2020; Holland & Powell, 2003). Thermolab currently has built in several internally consistent thermodynamic datasets for minerals, melts and fluids, the most extensive and up to date are the Holland and Powell endmember databases (Holland & Powell, 1998, 2011). The SUPCRT (dslop98) mineral database (Helgeson et al., 1978; Johnson et al., 1992) is implemented to allow calculations with additional minerals not included in the Holland and Powell datasets. For water (and/or CO_2), several equations of state (EOS) are implemented, including the EOS of the International Association for the Properties of Water and Steam

(IAPWS) (Wagner & Pruss, 2002, revised version, 2018), the EOS of Johnson and Norton (1991), Z. G. Zhang and Duan (2005), C. Zhang and Duan (2009), Pitzer and Sterner (1994), and the CORK EOS, from Holland and Powell (1991). For aqueous species, we have implemented the Holland and Powell (1998) formulation, and the Tanger and Helgeson (1988) formulation as implemented in SUPCRT92 (Johnson et al., 1992) using the 1998 database including more than 1300 aqueous species. Furthermore, it includes the Deep Earth Water (DEW) model (Sverjensky et al., 2014) with the recent updates and additional species from Huang & Sverjensky (2019), Aranovich et al. (2020) and the Miron dataset for aqueous species (Miron et al., 2016). This forms the endmember basis for use in thermodynamics of mixtures and for the local equilibrium calculations. In the future, this can be extended with additional thermodynamic endmember datasets. The following documents the main code as shown in an example in Figure 1.

3.1 Endmembers

The Gibbs energy of an endmember, e.g., a mineral, gas, fluid, or melt species with a fixed composition, is calculated from:

$$g^0 = g_r^0 - \int_{T_r}^{T} s \cdot dT + \int_{P_r}^{P} v \cdot dP + g_{ex}^0 \tag{4}$$

An internally consistent database contains the Gibbs energy at reference conditions ($g^0{}_r$). Alternatively, it holds enthalpy and entropy data from which the Gibbs energy at reference conditions can be obtained:

$$g_r^0 = h_r^0 - T_r \cdot s_r^0 \tag{5}$$

The entropy at constant pressure is evaluated from:

$$s^0 = s_r^0 + \int_{T_r}^{T} \frac{c_P}{T} \cdot dT \tag{6}$$

For every endmember, an expression for heat capacity and volume is needed to evaluate the above integrals and calculate the Gibbs energy.

3.1.1 Solids

An example of a heat capacity expression to be used in (6) consists of a four-parameter polynomial fit to experimental heat capacity data as used in the dataset of Holland and Powell (1998, 2011):

$$c_P = a + bT + cT^{-2} + dT^{-1/2} \tag{7}$$

For the pressure dependence of Gibbs energy an equation of state (EOS) is used to relate volume to pressure. For example, the Murnaghan equation of state used by Holland and Powell (1998):

$$P = P_r + \frac{K}{K'}\left[\left(\frac{v_r^0}{v^0}\right)^{K'} - 1\right] \quad (8)$$

```
clear,clf
% Input
T       = 995.3340;                                                    % T in Kelvin
P       = 0.2e9;                                                       % P in Pascal
solname = 'Amphibole';                                                 % Name of the phase
solfile = 'solution_models_H18';                                       % Solution model file name
Cname   = {'Si'  ,'Ti'  ,'Al'  ,'Ca',  'Fe',  'Mg',  'Na'  ,'K'   ,'H'   ,'O'    }; % System component names
Cmol    = [7.0006,0.1054,1.3603,1.6786,1.8705,2.9542,0.3382,0.0237,1.8946,24.0500]; % Composition in mol
% Load thermodynamic data
[p_id,st,site_id,mtpl,mod_id,alp,w,n_em,chg,em_data,dGex,EOS,CEOS,mcoef,Gr] = init_phase(solfile,solname,Cname);
% Water properties
rho_w   = rho_H2O(T,P,'ZD05');                                          % Water density (ZD05= Zhang & Duan (2005))
eps_di  = eps_H2O(T,P,rho_w,'S14');                                     % Dielectric constant (S14 = Sverjensky et al.2014)
% Endmember Gibbs energies
for k = 1:length(em_data)
    Gjp = zeros(1,size(em_data{k},1));                                  % Initialize G of make endmembers
    for jp = 1:size(em_data{k},1)                                       % For endmembers made of multiple phases
        [SdT,S]   = intSdT(T,P,em_data{k}(jp,:),CEOS{k}(jp));           % SdT integral
        [VdP,V]   = intVdP(T,P,em_data{k}(jp,:), EOS{k}(jp));           % VdP integral
        Gexc      = g0_exc(T,P,em_data{k}(jp,:),dGex{k}(jp),rho_w,eps_di); % dG of any fitting excess energy
        Gjp(:,jp) = Gr{k}(jp) - SdT + VdP + Gexc;                       % Equation 4
    end
    g0(k) = mcoef{k}*Gjp';                                              % Equation 11
end
% Prepare conversion matrices
[zt,zmax]                              = st2zt(st,site_id);             % Site fraction table
[p_from_c_cons,icomp_indep,isite_indep] = comp2prop(n_em',zt');          % C variables, p to C conversion matrix
% Grid for order-disorder
[z_od1,z_od2]                   = ndgrid(linspace(0,1,100),linspace(0,1,100)); % all possible order-disorder states
z_od                            = [z_od1(:),z_od2(:)];                  % order-disorder state matrix
% Proportions and site fractions
p  = (p_from_c_cons*[ones(length(z_od),1) repmat(Cmol(icomp_indep),length(z_od),1) z_od]')'; % Equation 37 (endmember proportions)
z  = p*zt;                                                              % Equation 16 (site fractions)
% Numerical
z_tol = 1e-10;z(z<1+z_tol & z>1-z_tol) = 1;z(z<  z_tol & z> -z_tol) = 1e-20;  % round off errors
badz  = min(z,[],2)<0|max(z,[],2)>1;p(badz,:) = [];z(badz,:) = [];           % remove unrealistic compositions
% Gibbs energy of mixing
g_mech = p*g0';                                                         % Mechanical mixing
g_id   = (T*8.3145*(mtpl*(z'.*log(z'+double(z'==0))- (zt'.*log(zt'+double(zt'==0)))*p')))'; % Ideal mixing
g_nid  = gnid(T,P,p,mod_id,V,alp,w,rho_w,eps_di,chg);                   % Non-ideal mixing
g      = g_mech + g_id + g_nid;                                         % Gibbs energy in Joule/mol
% Find stable configuration (homogeneous equilibrium)
[gmin,id] = min(g);                                                     % minimum of Gibbs energy
p(id,:)                                                                 % corresponding endmember proportions
```

Figure 1 *Thermolab code example to calculate the Gibbs energies of a phase for a given composition at fixed temperature (T) and pressure (P). Here the example for the amphibole model of Green et al. (2016). This code is a possible MATLAB translation of the equations and methods documented in the Gibbs energy calculation section of the main text. The first line in the code clears MATLAB memory and figure. In line 3 and 4 T and P are defined. Line 5 and 6 specify, respectively, for which phase to calculate the Gibbs energy and the name of the Excel file in which the solution model data is stored. Line 7 specifies the name of the elements in the phase, and line 8 the corresponding composition in moles for which to calculate the Gibbs energy. Line 10 is a call to read the needed thermodynamic data. Line 12 and 13 are needed for aqueous species and compute the density and dielectric constant of water. Line 15 to 24 compute the Gibbs energy of the endmembers in the solution (e. g. eq. 4&11). Proportions and site*

fractions are calculated in lines 26-33. Numerical errors are removed in lines 35 and 36. In Lines 29 and 30 a grid of all possible states of order-disorder is generated for the particular composition of the phase specified in line 8. For all these compositions the mechanical, ideal and non-ideal mixing energy is calculated in lines 38, 39, and 40, respectively. The non-ideal Gibbs energy, line 40, is a call to an external function that comprises a collection of non-ideal mixing functions that can be opted. Line 43 finds the Gibbs energy that is minimum and thus finds the state of order-disorder. Line 44 displays the corresponding proportions of the endmembers.

Note that the reference pressure is added to ensure the limit of standard reference conditions. The EOS can be rearranged for volume:

$$v^0 = v_r^0 \left[1 + \left(P - P_r \right) \left(\frac{K'}{K} \right) \right]^{-\frac{1}{K'}} \tag{9}$$

Substituting expression (6), and (9) into (4), and using a suitable heat capacity formula such as (7), the integrals can be evaluated analytically, or numerically. Lines 18-21 in Figure 1 show a MATLAB example of using equations (4), (5), and (6). In the example, the integrals in equation (4) are evaluated in a separate function. To use a different thermodynamic database, the heat capacity equation and EOS can be replaced by the appropriate expression. A number of important endmembers such as quartz are treated with additional volume and entropy terms to account for first or second order phase transitions such as heat capacity anomalies or order-disorder in the crystal lattice (e.g. sillimanite Holland & Powell, 1996). This then requires an excess Gibbs energy contribution, which in principle can also be calculated according to equation (4) using different volume and heat capacities and integration limits (e.g. Berman & Brown, 1985). Alternatively, an expression for this additional energy is given (Holland & Powell, 1998). In the example in Figure 1, this is represented by a call to a MATLAB function (line 20 in Figure 1). For the specific details we refer to the original papers documenting the internally consistent databases (Berman, 1988; Holland & Powell, 1998, 2011; Johnson et al., 1992).

3.1.2 Fluids

For molecular fluids such as H_2O and CO_2, the EOS, e.g. equation (8), is replaced by an appropriate fluid EOS. As water is one of the most important fluids on our planet, extensive work has been done on the thermodynamic formulation. The main difference between solids is that the fluid EOS, especially for water, usually cannot easily be rearranged for volume as there are multiple volumes possible for a single pressure in the region of coexisting fluid and gas. An example of this is given by the Modified Redlich Kwong (MRK) EOS, on which Holland and Powell (1991) base the fluid Gibbs energies to be compatible with the extensively used thermodynamically consistent dataset of Holland and Powell (1998):

$$P = \frac{RT}{v - b_{MRK}} - \frac{a_{MRK}}{v\left(v + b_{MRK}\right)\sqrt{T}} \tag{10}$$

Because this is a multivalued function a suitable algorithm must be used to calculate volume as function of P-T in the two-phase region (e.g. where gas and liquid coexist). In the single-phase region, the volume for the stable phase (gas or liquid) should be determined.

Holland and Powell (1991) rearranged the equation as a cubic in volume after which the correct root must be found in each phase region. Rather than solving which phase (e.g. gas, liquid, or both) is stable, the different regions were predefined and the correct volume was selected based on the P-T conditions. The MRK formulation in (10) is extended with a virial contribution and Holland and Powell (1991), give detailed instructions how to calculate the volume as function of P-T for H_2O, CO_2, and several other COH species. The advantage of the CORK formulation is that it can be integrated analytically and details in the original paper of Holland and Powell (1991) are sufficient for reproducing the values for use in Thermolab. The more updated thermodynamically consistent dataset of Holland and Powell (2011), that replaces the Holland and Powell (1998) dataset, uses the EOS of Pitzer and Sterner (1994).

Calculating the Gibbs energy of fluids then follows equation (4) just as for solids, with an entropy integral that is consistent with the dataset for solid, melt and/or gas endmembers. The Holland and Powell (1998, 2011) datasets have parameters for heat capacity, fitted simultaneously with the minerals to ensure the Gibbs energy at room pressure and elevated temperature can be calculated consistently.

In principle, the CORK or Pitzer and Sterner (1994) EOS can be used in conjunction with the SUPCRT mineral database, however for the entropy integral in (4) a consistent heat capacity formulation is needed to obtain thermodynamic calculations. The SUPCRT database does not contain heat capacity values for H_2O. The specific details needed for this calculation in the original papers of Johnson and Norton (1991) and Johnson et al. (1992) could not be found. Similarly, the DEW spreadsheet does not contain H_2O entries and combines Helgeson and Delaney (1978) and an internal routine for use only above at least 0.1 GPa, likely as it is intended to be used for Deep Earth applications. Moreover, at low P and T, e.g. for shallow processes, the CORK EOS should not be used (Holland and Powell, 1991). We found that by using the NIST Shomate heat capacity equations (Shomate, 1954), using parameters from the NIST website for liquid water and gas the Gibbs energies retrieved from SUPCRT can be reproduced accurately. The simplicity of the formulation and up to date online documentation of the parameters is of advantage. For calculations at elevated P, the numerical integration of the IAPWS or the EOS of Johnson and Norton (1991) give satisfactory results at low T, whereas the CORK EOS can be used above 100 °C (Holland and Powell, 1991).

3.1.3 Aqueous species

Gibbs energies of aqueous species are calculated in Thermolab following the formulation of Tanger and Helgeson (1988) as also outlined in Johnson et al. (1992). The resulting Gibbs energies have been compared to the output from SUPCRT and are reproduced within 1 Joule precision. The DEW model (Sverjensky et al., 2014) and the Miron dataset (Miron et al., 2016; Miron et al., 2017) use the same formulation, with refitted parameters for some of the endmember species. Although fundamentally the aqueous species are also calculated according to equation (4), there is a difference to the solid, melt and fluid endmembers because the aqueous species need the density and dielectric constant of the solvent. The contribution to Gibbs energy of solvation therefore needs the density and dielectric constant of water for the Born equation (Figure 1, Lines 12-13). This is included in the excess Gibbs energy term (Figure 1, Line 20). Note that in the example for amphibole in Figure 1, the properties of water are irrelevant, but to maintain some generality they have been left in the example. When computing the Gibbs energy of aqueous species, we change the name of the phase from Amphibole into any desired aqueous

304 species or fluid mixture defined in the solution model file. In Thermolab, the user can choose
305 from a number of EOS and dielectric constants to be used in the aqueous species Gibbs energy
306 (Fernández et al., 1997; Johnson & Norton, 1991; Sverjensky et al., 2014). The aqueous species
307 endmembers of Holland and Powell (1998) offers a restricted set of species compared to the
308 SUPCRT data, but it has the advantage that it is fitted in the internally consistent dataset of the
309 mineral, melt and gas endmembers of Holland and Powell (1998, 2011). Their formulation is
310 based on the Anderson density equation (Anderson et al., 1991) and uses the CORK EOS for the
311 water density. These aqueous species endmember data can also be used in fluid mixtures (Evans
312 & Powell, 2006, 2007).

313 3.1.4 Dependent endmembers

314 Endmembers can also be formed from a linear combination of several other endmembers
315 (Figure 1, Line 23):

316 $$g^0_{dep} = \boldsymbol{\nu} \cdot \mathbf{g^0} \tag{11}$$

317 where the $\boldsymbol{\nu}$ holds the stoichiometric reaction coefficients. A formation energy may be associated
318 with such a reaction and this can be captured in any functional form in the excess Gibbs energy
319 term of (4).

320 3.2 Gibbs energy of mixtures

321 The Gibbs energy of a phase (mineral, gas, fluid or melt species) that can form a mixture
322 between several endmembers is represented by the sum of mechanical, ideal, and non-ideal
323 mixing energies (Figure 1, Line 41):

324 $$g_{mix} = g_{mech} + g_{id} + g_{nid} \tag{12}$$

325 The mechanical part of the mixing is the sum of the Gibbs energy of all endmembers in
326 the mixture, weighted by their proportions (p) (Figure 1, Line 38).

327 $$g_{mech} = \mathbf{p} \cdot \mathbf{g}^0 \tag{13}$$

328 The ideal mixing Gibbs energy is given by a linear combination of the site fractions in the
329 mixture multiplied with their logarithm (Figure 1, Line 39):

330 $$g_{id} = R\,T\,\mathbf{m} \cdot \left(\mathbf{z} \ln\left(\mathbf{z}\right) - \mathbf{Z_t} \ln\left(\mathbf{Z_t}\right) \cdot \mathbf{p}\right) \tag{14}$$

331 The last term in equation (14) ensures that the ideal Gibbs energy is zero in the limit of
332 the pure endmember.

333 Non-ideal Gibbs energy can be calculated in the simplest way with a binary mixing
334 formula:

335 $$g_{nid} = \mathbf{p^T} \cdot \mathbf{W} \cdot \mathbf{p} \tag{15}$$

336 This is essentially a sum of multiplications of binary pairs of endmembers in the mixture
337 multiplied with their interaction parameters. These interaction parameters can depend on
338 composition to get an asymmetric mixing formulation, referred to as subregular mixing model

(Ganguly, 2020). When **p** is replaced with a size parameter adjusted proportion and using the appropriate **W** the asymmetric formulism of Holland and Powell (2003) can be used. If the molar volumes of the endmembers are used as size parameter, it is essentially a Van Laar mixing model (Van Laar, 1906), as for example used by Aranovich and Newton (1999). The **W** and any size parameters are in general also temperature and pressure dependent such as also the molar volume used in Van Laar mixing models. Any other regular or subregular solution models can be used in place of (15) and ternary interaction terms may be added. In Thermolab, it is possible to expand the codes with a variety of mixing formulas for the non-ideality by adding the appropriate formulation to the function called in line 40 in Figure 1.

3.3 Solution models

The data for **m**, and $\mathbf{Z_t}$ are retrieved from a site occupancy table, stored for example in an Excel spreadsheet. In this spreadsheet, also data for **W** and any size parameters for asymmetric formalism models (Holland & Powell, 2003) and the model type are stored. In Figure 1, the data is loaded in the beginning of the code (line 10, Figure 1) from a function that reads the Excel data. Site fractions **z** are obtained by multiplying the transpose of the site fraction speciation matrix with a column vector of proportions:

$$\mathbf{z} = \mathbf{Z_t}^T \cdot \mathbf{p} \tag{16}$$

After specifying proportions of the endmembers in a solution, the Gibbs energy of that particular phase and composition at a given P and T can be calculated from the above.

3.3.1 Site occupancy

The site occupancy of the mixture can be represented by a table listing the occupancy of crystallographic sites for each endmember. For example a binary olivine solution with only one crystallographic site M, and a fixed silica tetrahedral site (which has composition SiO_4), is shown in Table 2. It can be represented by a matrix:

$$\mathbf{S_t} = \begin{bmatrix} 2 & 0 & 1 \\ 0 & 2 & 1 \end{bmatrix} \tag{17}$$

Table 2. Binary olivine site occupancy

Site	M		T
Occupancy	*Mg*	*Fe*	*SiO_4*
Endmember			
Forsterite	2	0	1
Fayalite	0	2	1

The columns represent occupancy of each species on a crystallographic site for the endmember in the rows of the table. Site fractions **z** can be retrieved from this table by dividing each site occupancy over the sum of moles of the species on that site, which gives the site multiplicity, and can be represented by a vector:

$$\mathbf{m} = \begin{bmatrix} 2 & 2 & 1 \end{bmatrix} \tag{18}$$

Elementwise division of each row in Table 2 or in matrix (17) with this multiplicity vector leads to a table of site fractions represented by the matrix:

$$\mathbf{Z}_\mathbf{t} = \begin{bmatrix} 1 & 0 & 1 \\ 0 & 1 & 1 \end{bmatrix} \tag{19}$$

Table 3. Binary olivine site fraction table

Site	M		T
Occupancy	*Mg*	*Fe*	*SiO_4*
Site multiplicity	*2*	*2*	*1*
Endmember			
Forsterite	1	0	1
Fayalite	0	1	1

Using (16) and spelling this out in matrix-vector notation, it is essentially a set of equations where the coefficients in front of the proportions are directly read from the site fraction table and then transposed:

$$\begin{bmatrix} z^M_{Mg} \\ z^M_{Fe} \\ z^T_{SiO_4} \end{bmatrix} = \begin{bmatrix} 1 & 0 \\ 0 & 1 \\ 1 & 1 \end{bmatrix} \begin{bmatrix} p_{fo} \\ p_{fa} \end{bmatrix} \tag{20}$$

The site fractions become:

$$\begin{aligned} z^M_{Mg} &= p_{fo} \\ z^M_{Fe} &= p_{fa} \\ z^T_{SiO_4} &= p_{fo} + p_{fa} \end{aligned} \tag{21}$$

3.3.2 Ordering

In fact, in olivine, Mg and Fe can interchange on two molecular sites M1 and M2. We could rewrite the site speciation table. However using only the two endmembers, it would not lead to a different configurational entropy. There needs to be an endmember that allows different distribution of Mg and Fe on the two sites. This is the purpose of introducing an ordered endmember e.g. “Ordered Olivine”. The Gibbs energy of this endmember can be made out of two endmembers, forsterite and fayalite and an energy of reaction may be added.

After this, we get three proportions that define the Gibbs energy. In principle, the endmember could also be formulated as having all Fe on M1 and all Mg on M2, however using a negative proportion of the ordered olivine listed in the table we can also reach this result (Powell & Holland, 1999).

Using the speciation matrix and (16) we get:

$$\begin{bmatrix} z_{Mg}^{M1} \\ z_{Fe}^{M1} \\ z_{Mg}^{M2} \\ z_{Fe}^{M2} \\ z_{SiO_4}^{T} \end{bmatrix} = \begin{bmatrix} 1 & 0 & 1 \\ 0 & 1 & 0 \\ 1 & 0 & 0 \\ 0 & 1 & 1 \\ 1 & 1 & 1 \end{bmatrix} \begin{bmatrix} p_{fo} \\ p_{fa} \\ p_{od} \end{bmatrix} \quad (22)$$

Giving the site fractions:

$$\begin{aligned} z_{Mg}^{M1} &= p_{fo} + p_{od} \\ z_{Fe}^{M1} &= p_{fa} \\ z_{Mg}^{M2} &= p_{fo} \\ z_{Fe}^{M2} &= p_{fa} + p_{od} \\ z_{SiO_4}^{T} &= p_{fo} + p_{fa} + p_{od} \end{aligned} \quad (23)$$

3.3.3 Worked example

Using the multiplicities and site fractions for the olivine example we get using Equation (14):

$$g_{id} = R\,T\,2\left(z_{Mg}^{M} \cdot ln\left(z_{Mg}^{M}\right) + z_{Fe}^{M} \cdot ln\left(z_{Fe}^{M}\right)\right) \quad (24)$$

The non-ideal mixing energy becomes:

$$g_{nid} = \left(\, w_{fo,fa} + w_{fa,fo}\right) p_{fo}\, p_{fa} \quad (25)$$

In case we use a Holland and Powell (1998) model for olivine, the non-ideal parameters are equal to each other and reduces to the simple binary symmetric mixing parabola:

$$g_{nid} = 2w_{fo,fa}\left(1 - p_{fo}\right) p_{fo} \quad (26)$$

For the example with order-disorder the ideal mixing Gibbs energy becomes:

$$g_{id} = R\,T\left(z_{Mg}^{M1}\, ln\left(z_{Mg}^{M1}\right) + z_{Fe}^{M1}\, ln\left(z_{Fe}^{M1}\right) + z_{Mg}^{M2}\, ln\left(z_{Mg}^{M2}\right) + z_{Fe}^{M2}\, ln\left(z_{Fe}^{M2}\right)\right) \quad (27)$$

(Note that the T-site fraction cancels due to the logarithms because the site fraction is always 1).

The non-ideal Gibbs energy becomes:

$$g_{nid} = \left(w_{fo,fa} + w_{fa,fo}\right) p_{fo}\, p_{fa} + \left(w_{fo,od} + w_{od,fo}\right) p_{fo}\, p_{od} + \left(w_{fa,od} + w_{od,fa}\right) p_{fa}\, p_{od} \quad (28)$$

3.3.4 Proportions from site fractions

The proportions can be written as function of site fractions by solving the system of equations in (23) using the independent equations and the fact that proportions sum up to 1. This leads to:

$$\begin{aligned} z_{Fe}^{M1} &= p_{fa} \\ z_{Mg}^{M2} &= p_{fo} \\ p_{fo} + p_{fa} + p_{od} &= 1 \end{aligned} \tag{29}$$

Which after solving for proportions gives:

$$\begin{aligned} p_{fa} &= z_{Fe}^{M1} \\ p_{fo} &= z_{Mg}^{M2} \\ p_{od} &= 1 - z_{Fe}^{M1} - z_{Mg}^{M2} \end{aligned} \tag{30}$$

Hence, there are two independent site fractions together completely defining the composition and ordering of the olivine in this example.

3.3.5 Proportions from composition

From the olivine table we can derive a list of compositions of each endmember by summing up the moles of each atom over the sites.

Again, this table can serve to set up a system of equations and may be added by the constraint that the sum of the proportions equals 1 (first equation):

$$\begin{bmatrix} 1 & 1 & 1 \\ 2 & 0 & 1 \\ 0 & 2 & 1 \\ 1 & 1 & 1 \end{bmatrix} \begin{bmatrix} p_{fo} \\ p_{fa} \\ p_{od} \end{bmatrix} = \begin{bmatrix} 1 \\ Mg \\ Fe \\ SiO_4 \end{bmatrix} \tag{31}$$

However, this table only has 2 independent equations (rank = 2). We need another equation to solve for all three proportions. A simple solution could be to treat the ordered endmember as a known variable on the right hand side. Our extended system can be written:

$$\begin{bmatrix} 1 & 1 & 1 \\ 2 & 0 & 1 \\ 0 & 2 & 1 \\ 1 & 1 & 1 \\ 0 & 0 & 1 \end{bmatrix} \begin{bmatrix} p_{fo} \\ p_{fa} \\ p_{od} \end{bmatrix} = \begin{bmatrix} 1 \\ Mg \\ Fe \\ SiO_4 \\ p_{od} \end{bmatrix} \tag{32}$$

Starting from the first required equation and adding equations until we have reached the rank of the matrix gives us directly the first 2 and the last equation. This means the set of independent equations becomes:

$$\begin{bmatrix} 1 & 1 & 1 \\ 2 & 0 & 1 \\ 0 & 0 & 1 \end{bmatrix} \begin{bmatrix} p_{fo} \\ p_{fa} \\ p_{od} \end{bmatrix} = \begin{bmatrix} 1 \\ Mg \\ p_{od} \end{bmatrix} \tag{33}$$

The matrix in (33) can be inverted and used to find the expressions for the endmember proportions as function of composition:

$$\begin{bmatrix} 0 & 0.5 & -0.5 \\ 1 & -0.5 & -0.5 \\ 0 & 0 & 1 \end{bmatrix} \begin{bmatrix} 1 \\ Mg \\ p_{od} \end{bmatrix} = \begin{bmatrix} p_{fo} \\ p_{fa} \\ p_{od} \end{bmatrix} \tag{34}$$

Instead of varying the ordered endmember proportion, it is also possible to vary one of the site fractions. For example, we can have the site fraction of Fe on M2 as variable in addition to the compositional variables. This way, we can fix the bulk composition of the mineral while varying the site occupancies due to ordering. To this end, we add the equation for site fraction of Fe on M2 (from equation (23)), to the original system of equations:

$$\begin{bmatrix} 1 & 1 & 1 \\ 2 & 0 & 1 \\ 0 & 2 & 1 \\ 1 & 1 & 1 \\ 0 & 1 & 1 \end{bmatrix} \begin{bmatrix} p_{fo} \\ p_{fa} \\ p_{od} \end{bmatrix} = \begin{bmatrix} 1 \\ Mg \\ Fe \\ SiO_4 \\ z_{Fe}^{M2} \end{bmatrix} \tag{35}$$

Here only the first, second, and last equation are independent and so we have:

$$\begin{aligned} p_{fo} + p_{fa} + p_{od} &= 1 \\ 2p_{fo} + p_{od} &= Mg \\ p_{fa} + p_{od} &= z_{Fe}^{M2} \end{aligned} \tag{36}$$

Solved for the three unknown proportions:

$$\begin{aligned} p_{fo} &= 1 - z_{Fe}^{M2} \\ p_{fa} &= 2 - Mg - z_{Fe}^{M2} \\ p_{od} &= Mg + 2z_{Fe}^{M2} - 2 \end{aligned} \tag{37}$$

These equations guarantee a fixed olivine composition, while changing the distribution of Fe and Mg on M1 and M2. The site fraction equation to pick as order equation can be obtained by augmenting the system of equations in (35) with the site fraction equations in (23). Then from this complete set of equations, we pick only the independent ones by starting from the first equation in (35) and adding only equations that increase the rank of the system of equations. Taking as first equation that the sum of proportions add to one (first row in eq. (35)), is convenient as it guarantees the minimum amount of compositionally independent variables. A Matlab code that automates this procedure is used in Thermolab. This function gives the

independent components for each solution model as well as the site fraction to vary as order parameter and the matrix of converting composition to proportion.

For any given composition, there are limits on the value of z^{M2}_{Fe}. The easiest to see that not any value between 0 and 1 is possible is to take pure forsterite, where Mg = 2. Then there is no Fe in the olivine, and therefore z^{M2}_{Fe} can only be 0. In Thermolab, the range of possible values for site fractions is found by generating the full range of values and discarding impossible site fractions (below 0 and above 1).

We note that it is also possible to calculate site fractions from bulk composition as is shown in the Appendix in Vrijmoed and Podladchikov (2015).

3.2.6 Aqueous fluids

For mixtures of aqueous species, an approach similar to the ideal olivine example can be taken. Treating the fluid mixture with a one-site model in which all species mix in a similar fashion the mechanical and ideal mixture is calculated as in equation (13) and (14), and for the non-ideality, the Helgeson Kirkham Flowers (HKF) extended Debye-Hückel activity is used (Dolejš & Wagner, 2008; Helgeson et al., 1981). The Gibbs energy of the fluid mixture are on a molality scale when the formulation of Johnson et al. (1992) and the HKF activity model (Helgeson et al., 1981) is used and must be converted to a molar based scale as in Dolejs (2013) to be compatible with the solids. This is taken care by adding a correction term in the non-ideal Gibbs energy.

4 Equilibrium calculations using reactions

Gibbs energies calculated with the Thermolab codes are benchmarked with THERMOCALC (Holland & Powell, 2011), SUPCRT92 (Johnson et al., 1992), the DEW spreadsheet (Sverjensky et al., 2014) or data and phase diagrams from the relevant publications (Miron et al., 2016) and Perple_X (Connolly, 2005). Additionally, comparing with experimental data is essential to increase confidence in the method.

With the Gibbs energies of endmembers, equilibrium conditions for simple reactions can be calculated. Results for several solid state and fluid-solid reactions are shown Figure 2. The curves are produced by making use of the equilibrium condition:

$$0 = \Delta G_{rxn}^{\ 0} + RT \ln(K_{eq}) \tag{38}$$

For pure phases (e.g. endmembers), the equilibrium constant will be 1 and the logarithmic term disappears leaving only $\Delta G^0_{rxn} = 0$. Using the endmember Gibbs energies and stoichiometric coefficient of reactions the contour line of $\Delta G^0_{rxn} = 0$ can be plotted to visualize the reaction in P-T space (Figure 2a). In a simple dissolution reaction K_{eq} will be equal to solubility and so we can use ΔG^0_{rxn} to calculate the solubility of quartz (Figure 2b). An example of a single dissociation reaction is shown in Figure 2c. By varying activities in K_{eq} and using them as axis on a diagram the contour lines where the right hand side is 0 are used to obtain an activity-activity plot (Figure (2d).

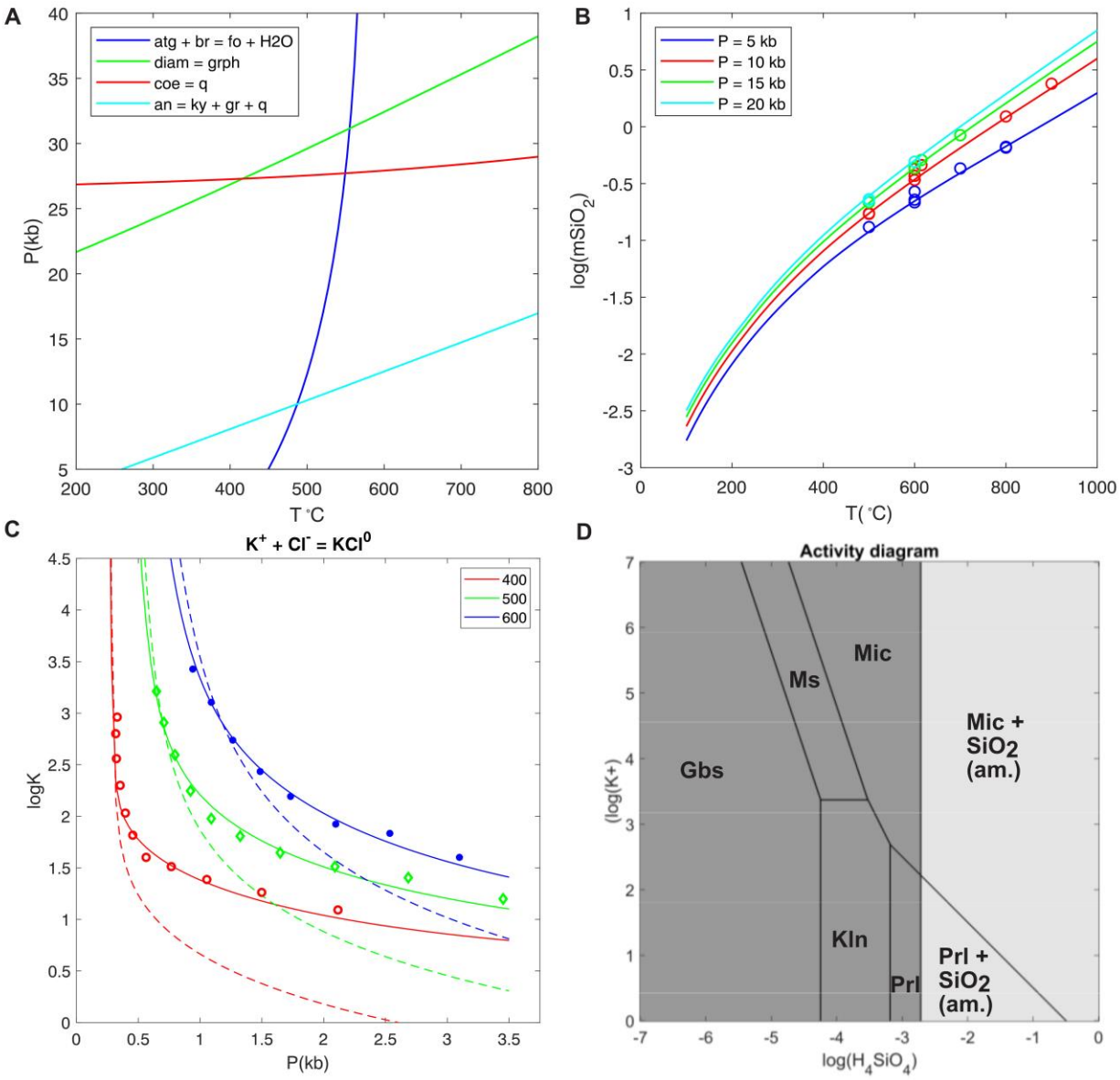

Figure 2 *Example equilibrium calculations using a basic chemical reaction approach.* ***a)*** *Examples of some well-known reactions between pure phases, by calculating ΔG of reaction (including any metastable parts of reactions).* ***b)*** *Solubility of aqueous silica, by plotting the*

equilibrium constant of the dissolution of quartz into water using the Holland and Powell (1998) database. Comparison between data from Manning (1994) shows good agreement between model and experiment. ***c)*** *Comparison between experimental data and the SUPCRT (dashed lines) and Miron (solid lines) dataset for the dissociation of KCl in water. This reproduces the figure shown by Miron et al. (2016), to demonstrate their improved fit to the data.* ***d)*** *Activity diagram at room pressure, temperature, for basic weathering reactions using the equilibrium constants of the reaction calculated with Thermolab using the (dslop98) SUPCRT aqueous species and minerals data and Gibbs energy of water from NIST. Here a procedure to remove metastable extensions of reactions is performed in an automated way (i.e. automated Schreinemakers analysis). Gbs= Gibbsite, Ms = Muscovite, Mic = Microcline, Kln= Kaolinite, Prl = Pyrophyllite, SiO2 (am.) = amorphous silica.*

5 Gibbs minimization in MATLAB

Using the ΔG of reaction, the metastable part of individual reactions will also be plotted (e.g. Figure 2a). For an equilibrium phase diagram, a Schreinemakers analysis or similar procedure may follow to draw the stable reactions (e.g. Figure 2d). Additionally, the phases and reactions to be calculated must be known beforehand. However, in many cases it can be desired to predict which reactions may take place. Instead of predicting the equilibrium line of a chemical reaction we calculate the stable phase assemblage at a point in P-T by determining which mineral has the minimum Gibbs energy. In the example code (Figure 3A), the calculation of Gibbs energy of the endmembers is done in line 9, a call to the main Thermolab function, which includes the code in Figure 1 to focus on the minimization algorithm. If all phases have the same composition (i.e. they are polymorphs), then the “min” function can be used (Figure 3A&B). Instead of locating the coexisting phases in a reaction in P-T-X space, the Gibbs minimization delivers the stable phases everywhere except for on the reaction line. Therefore, the reaction lines reflect the resolution of the P-T grid for which the Gibbs energies of each phase are calculated. At sufficiently high resolution, the reaction lines become smooth.

Natural chemical systems, e.g., rocks, generally, are multi-component systems. In this case mass balance must be considered while finding the minimum of Gibbs energy. For a more thorough thermodynamic analysis of this see e.g. Connolly (2017). Constrained Gibbs energy minimization is employed in the majority of phase diagram calculation software (Connolly, 2009; Gordon & McBride, 1994). In MATLAB, the simplest way this can be achieved is using linear programming (function "linprog", e.g. Dantzig et al., 1955). With this function, minimization can be done under the constraints of mass balance equalities, which for completeness is shortly outlined in the following.

The function “linprog” is used to find the minimum Gibbs energy of the system by solving the following optimization problem,

$$\min(G_{sys}) = \mathbf{g} \cdot \boldsymbol{\alpha} \tag{39}$$

where $\boldsymbol{\alpha}$ and $\mathbf{g}$ are vectors of respectively, the molar amount, and the Gibbs energies of all phases. The “linprog” algorithm then searches for the components in $\boldsymbol{\alpha}$ that make the minimum Gibbs energy of the system, while respecting the following mass balance equality:

$$\mathbf{n_{sys}} = \mathbf{N_{phs}} \cdot \boldsymbol{\alpha} \tag{40}$$

Which state that the sum of the amount of each phase multiplied by the composition of a component should equal the sum of that component in the system. A final requirement is that no negative amount $\boldsymbol{\alpha}$ is allowed as that is physically meaningless:

$$\boldsymbol{\alpha} \geq 0 \tag{41}$$

A

```
1 clear,clf
2 % Input
3 T          = linspace(300,800,200)+ 273.15;               % Temperature (K)
4 P          = linspace(0.1e9,1e9,200);                     % Pressure (Pa)
5 phase      = {'ky,tc-ds55','sill,tc-ds55','and,tc-ds55'}; % Phase name
6 % Numerics
7 [T2d,P2d]  = ndgrid(T,P);                                 % Create P-T grid
8 % Gibbs energy function
9 g          = tl_gibbs_energy(T2d(:),P2d(:),phase);        % G (J/mol)
10 % Find minimum of Gibbs energy and stable phase index (ind)
11 [gmin,ind] = min(g);
12 % Visualize stable phase
13 pcolor(T2d,P2d,reshape(ind,length(T),length(P))),colorbar,shading flat
```

Published with MATLAB® R2020b

B

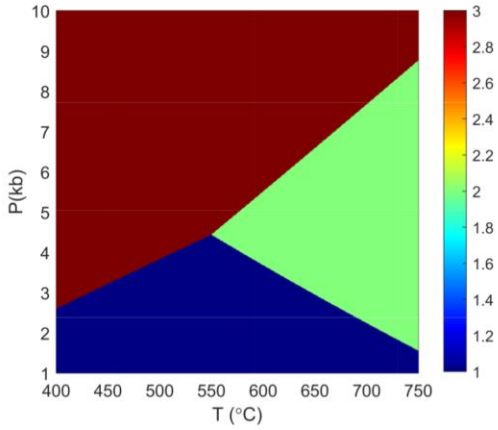

C

```
1 clear,clf
2 % Input
3 T      = 1000+ 273.15;     % Temperature (K)
4 P      = 0.1e9;            % Pressure    (Pa)
5 phase = {'q,tc-ds55','per,tc-ds55','en,tc-ds55','fo,tc-ds55'};  % Phase name
6 g      = tl_gibbs_energy(T,P,phase);
7 Nsys = [1.2  % Si in system
8         2.0  % Mg in system
9         4.4];% O  in system
10 Nphs = [1 0 2 1  % Si in phases
11         0 1 2 2  % Mg in phases
12         2 1 6 4];% O  in phases
13 LB   = zeros(1,length(g));            % lower bounds for linprog minimization
14 alph = linprog(g,[],[],Nphs,Nsys,LB); % constrained Gibbs energy minimization
```

Published with MATLAB® R2020b

D

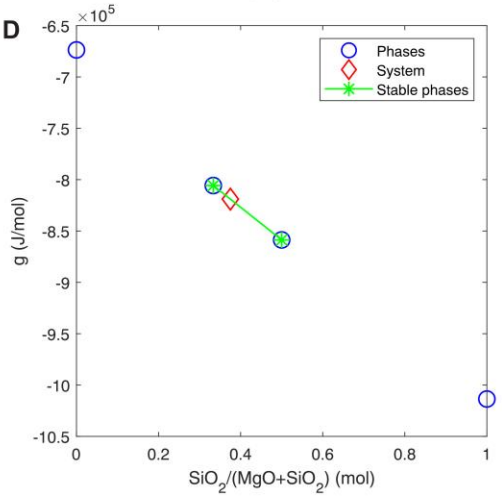

Figure 3 *Two examples of Gibbs minimization to calculate phase equilibrium with Thermolab. The Gibbs energy calculation shown in Figure 1 is used here as an external function to improve clarity of the algorithm.* ***a)*** *Code showing unconstrained Gibbs minimization used to calculate the aluminosilicate phase diagram. The Gibbs energies of the phases are obtained in line 9, using a unique identifier to distinguish them from the same phases in another database. Andalusite from the tc-ds55 THERMOCALC (Holland & Powell, 1998) dataset (and, tc-ds55), kyanite (ky,tc-ds55) and sillimanite (sill,tc-ds55) in the order in which they are specified in line 5. The result is a 3D array with T in first dimension, P in second dimension and phase in third dimension. Line 11 then finds the minimum in the 3rd dimension, which results in a value (val) and index (ind) for each P-T. The index corresponds to the list of phases in line 5. A color coded visualization of the phase index that gives the lowest Gibbs energy is shown to the right using the pcolor function in MATLAB (code: line 13). The color bar indicates that the blue area has index 1, which then means it is the first phase in the list (line 5) that is stable (i. e. 1= andalusite, 2= kyanite, 3=sillimanite). The resolution of phase diagram can be increased by decreasing the step*

size of temperature and pressure (line 3&4). ***b)*** *Resulting plot from code in (a).* ***c)*** *MATLAB example to calculate chemical equilibrium using constrained Gibbs energy minimization. For the first lines see (a). In line 7-8 the system composition is specified using total moles of SiO_2 and MgO. Then the phase compositions in moles is expressed in the matrix N_{phs} with in each column the phase corresponding to the list in line 5. Each row holds the components (SiO_2, MgO). This information is used as equality constraints in the function linprog which is called in line 14. It then finds the minimum Gibbs energy of the system out of the 4 possible phases, while satisfying the equality constraints. The second and third input arguments for 'linprog' are empty as they are reserved for inequalities and the fourth and fifth arguments are for the matrix of coefficients and right-hand side vector, respectively. To restrict the linear programming search for the amount of each phase to positive values we input also the lower bound vector of zeros (LB), e.g. equation* (41)*. Then alph will hold the amount of each phase that will make minimum system Gibbs energy while obeying system composition. The phases that have an alph above zero represent the equilibrium assemblage for the given P-T-X conditions.* ***d)*** *G-X diagram in which the Gibbs energy of the phases are plotted against system composition (for plotting the Gibbs energy is normalized over the sum of the moles of component in each phase: i.e. the sum over the rows of N_{phs}).*

As a worked example we may consider the binary system SiO_2-MgO. Possible phases that can be built from these components are quartz, periclase, enstatite, forsterite. Spelled out for this case the equations read in matrix form:

$$\min(G_{sys}) = \begin{pmatrix} g_{qtz} & g_{per} & g_{en} & g_{fo} \end{pmatrix} \begin{pmatrix} \alpha_{qtz} \\ \alpha_{per} \\ \alpha_{en} \\ \alpha_{fo} \end{pmatrix} \tag{42}$$

And

$$\begin{pmatrix} N_{sys,SiO_2} \\ N_{sys,MgO} \end{pmatrix} = \begin{pmatrix} N_{qtz,SiO_2} & N_{per,SiO_2} & N_{en,SiO_2} & N_{fo,SiO_2} \\ N_{qtz,MgO} & N_{per,MgO} & N_{en,MgO} & N_{fo,MgO} \end{pmatrix} \begin{pmatrix} \alpha_{qtz} \\ \alpha_{per} \\ \alpha_{en} \\ \alpha_{fo} \end{pmatrix} \tag{43}$$

Figure 3c shows the MATLAB translation and usage of "linprog" (Figure 3c, line 14) to calculate the stable phase assemblage. The required known values for the minimization are the vector of Gibbs energies (Figure 3c, line 6), a vector of system compositions (Figure 3c, line 7) with matrix of mineral compositions (Figure 3c line 10-12) as in equation (43). Note that in Figure 3C single elements have been used as components instead of the oxides, which leads to the same result. After defining the lower bounds of alpha's as zero, linprog finds the alpha's that make the minimum of Gibbs energy. The results are plotted in Figure 3d and shows that for a system composition between enstatite and forsterite, alpha's of enstatite and forsterite are non-zero which means that those are the stable phases and the magnitude of the alpha's give the molar amount of each stable phase in order of definition of the list of phases in Figure 3c, line 5.

Performing a minimization at each point in a grid of pressure and temperature and evaluating at each P-T point the stable phase assemblage leads to a phase diagram in which also the amount of each phase is known because of the mass balance constraint. Figure 4a shows that this produces the same result in case of the pure Al_2SiO_5 system, as in the unconstrained minimization, but that it can now be used to do multi-component systems such as dehydration of antigorite in SiO_2, MgO, H_2O (Figure 4b).

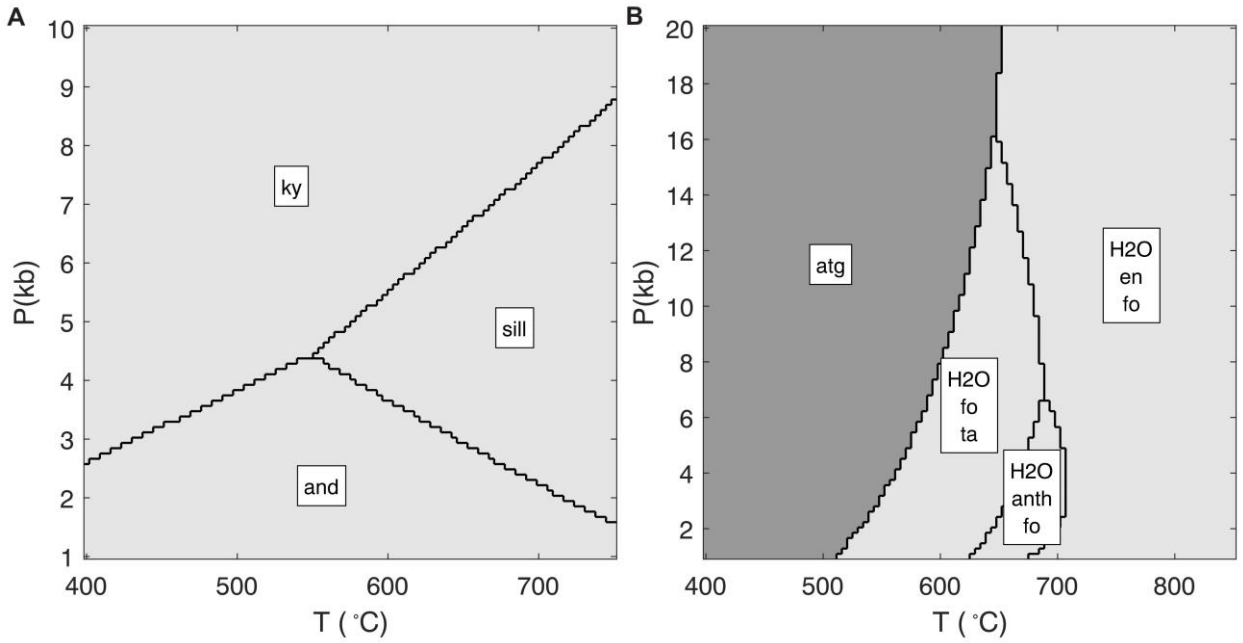

Figure 4 ***a)*** *One component system phase diagram, using constrained Gibbs minimization, results in a similar diagram to the unconstrained minimization result for the aluminosilicate phase diagram in Figure 3.(ky=kyanite,sill=sillimanite,and=andalusite)* ***b)*** *Multicomponents system phase diagram, with pure phases, using components SiO_2, MgO, H_2O. The same code is used as in (a), only the composition and system components need modification (atg = antigorite,fo=forsterite,ta=talc,anth=anthophyllite).*

Most minerals, fluid and melts are not just pure phases, but can form mixtures of endmembers. The basic example above is shown because essentially the Gibbs minimization approach used in Thermolab is the same for systems in which phases occur that have a variable composition. In the following we shortly outline how we approximate the equilibrium in Thermolab to a reasonable degree by using the same linear programming method.

5.1 Linearization of mixtures

We compute the Gibbs energy of a set of discrete compositions of the mixture and add them to the list of endmembers as discrete entities, being treated as a fixed composition phase. In the following, all these entities that are the consequence of discretizing a real phase that can form a thermodynamic mixture will be arbitrarily called phase-compounds. With this approach the minimization algorithm remains unchanged from the above case for pure phases in Figure 3c. Figure 5 shows a complete code example to do a calculation with mineral solid solutions using the approach described here.

```
1 clear
2 runname = 'example_soap';
3 T       = 300 + 273.15;                                          % T in Kelvin
4 P       = 0.3e9;                                                 % P in Pascal
5 solfile = 'solution_models_soapstone';                           % Name of solution model file
6 Cname   = {'Si'  ,'Al'  ,'Mg'  ,'Fe',  'Ca',  'C',   'H'   ,'O'   ,'e'}; % Components in the system
7 Xsys    = [0.7392;0.0451;1.0000;0.0644;0.0113;0.0232;1.3895;3.3629; 0];  % moles of each component in system
8 fluid   = 'Fluid-CO2-H2O(DEW)';                                  % Name of fluid model
9 phases  = {fluid,'Chlorite','Antigorite','Clinopyroxene','Talc','Magnesite','Dolomite','Brucite','Olivine',...
10           'per,tc-ds55','q,tc-ds55','ky,tc-ds55','sill,tc-ds55','and,tc-ds55'}; % Names of phases to consider
11 td      = init_thermo(phases,Cname,solfile);                     % Initialize phase data
12 p       = props_generate(td);                                    % Grid of compositions for mixtures
13 rho_w   = rho_H2O(T,P,'ZD05');                                   % Density of water
14 eps_w   = eps_H2O(T,P,rho_w,'S14');                              % Dielectric constant
15 [g0,v0] = tl_g0(T,P,td,rho_w,eps_w);                             % Endmember g and v in mixture
16 % Compute Gibbs energy
17 [g,Npc,pc_id] = tl_gibbs_energy(T,P,phases,td,p,g0,v0,rho_w,eps_w);  % Call Gibbs energy function
18 % Gibbs minimization
19 LB     = zeros(1,length(g));                                    % stable phase amount cannot be negative.
20 alph   = linprog(g,[],[],Npc,Xsys,LB);                          % The Gibbs energy minimization
21 % Save results
22 save([runname '_linprog']);
```

Figure 5. *Complete example code for the calculation of chemical equilibrium using Gibbs energy minimization including solid solutions, aqueous species and pure phases in Thermolab for the case of serpentinite with addition of carbon (Beinlich et al., 2020). After defining a P and T of interest, the solution model Excel spreadsheet is selected (line 5). The chemical components in the system are defined in line 6 and the composition of the system is specified in line 7. The names of the phases to be considered in the calculation are specified in lines 8-10, where the tc-ds55 identifies the thermodynamic dataset to be used (here THERMOCALC dataset 55). The static thermodynamic data (td) for all phases are loaded in line 11 and stored in one structure array (this replaces the command in Figure 1, line 10). The grid of compositions to linearize the solutions is obtained in line 12. Lines 13-14 compute the density (ZD05 = Z. G. Zhang & Duan, 2005) and dielectric constant of water (S14 = Sverjensky et al., 2014). Line 15 computes the Gibbs energy and volumes of the endmembers in each solution. Line 17 is the call to the main function outlined in Figure 1, and calculates for all phases in the list the Gibbs energy (g), the composition of each phase compound (Npc), an identifier for each phase compound (pc_id. Line 20 performs the constrained Gibbs minimization and in line 22 the data is stored for postprocessing.*

An important step in preparing the mixtures for Gibbs minimization is to generate a grid holding a set of discrete phase compositions representing the mineral, fluid, melt, or gas. The compositions need to cover the full range of possible site fractions or proportions that can exist for a mixture. Fixing the pressure and temperature, Gibbs energy can be calculated either by specifying the site fractions or the proportions. The simplest is to use the site fractions for grid generation because they range from zero to one. Using proportions is more complex because, although proportions sum up to one for each mixture, they can also be negative. Thus, it requires knowledge of the range of values for proportions in each different solution. The grid generation is done in the function call in Line 12, Figure 5, by varying the site fractions by default from 0 to 1, and generating a multi-dimensional cartesian grid over the correct number of independent site fractions, using the MATLAB function “ndgrid” inside. With this brutal way, many non-physical site fractions are generated, but these are removed inside the grid generation function. In summary, we just generate Gibbs energies for the full range of possible site fractions in the

solution including all states of ordering and internal speciation. The resulting set of Gibbs energies and compositions is used in place of the example in Figure 3c. The call to the main code 'tl_gibbs_energy', in Figure 5 Line 17, now includes the complete Gibbs energy code example Figure 1.

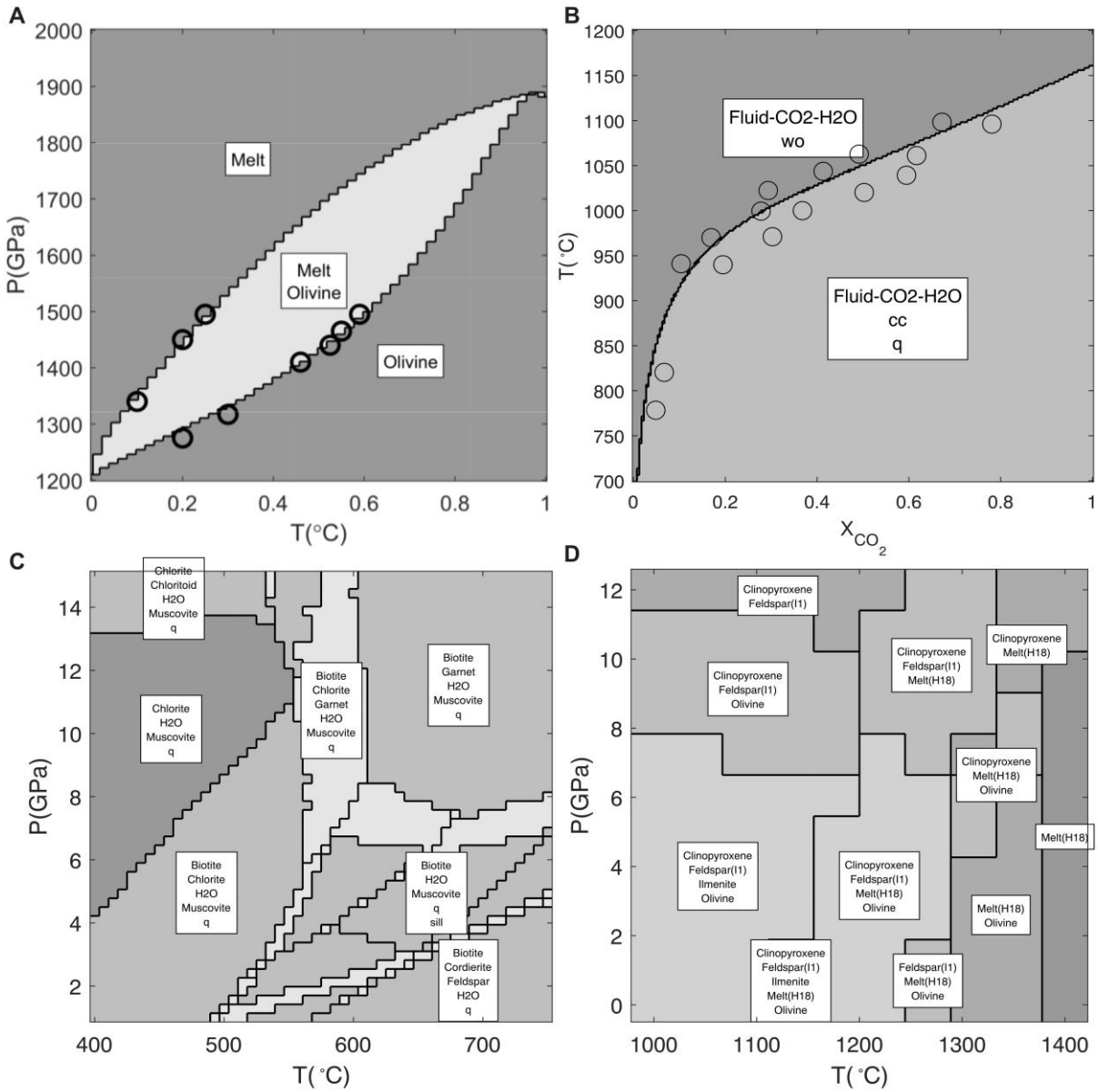

Figure 6 ***a)*** *T-X diagram for the binary system fo-fa, with olivine and melt as mixtures using the Holland and Powell (2011) dataset and solution model for olivine from Holland et al. (2018) and melt using the example from the text and by adapting the Margules parameters to fit the Bowen and Schairer (1935) experiments.* ***b)*** *T-X_{CO2} diagram for CaO-SiO_2-H_2O-CO_2 system at 14 kbar. Data points from Aranovich and Newton (1999) as benchmark to the Gibbs energy and minimization approach in Thermolab.* ***c)*** *Benchmark KFMASH metapelite example using the*

composition from the code in Figure 5. Solution models: Chlorite (Holland et al., 1998), Chloritoid, Cordierite (Holland & Powell, 1998), Muscovite (Coggon & Holland, 2002), Garnet, Biotite (R. W. White et al., 2007). ***d)*** *Basalt melting to benchmark the Holland et al. (2018) melting model by reproducing main topology in Fig. 5 of Holland et al. (2018), here calculated in SiO_2-TiO_2-Al_2O_3-MgO-FeO-CaO-Na_2O.*

As an example of including solutions, we show a variety of phase diagrams, all produced with the same code for a discrete set of P-T values. The first example in Figure 6a, applies the olivine solution model as described above together with a binary melt mixing model, replacing the solid endmembers with their liquid equivalents (liquid forsterite and fayalite). For olivine, a grid is created where z_{Fe}^{M1} and z_{Mg}^{M2} vary independently and for the melt, the site fraction of forsterite liquid is varied. The Margules parameters in the melt are adjusted until they fit the experimental data (Bowen & Schairer, 1935). The T-X diagram including CO_2 fluid using the mixing model of Aranovich and Newton (1999) is produced by changing the bulk CO_2 in the system. When the amount of fluid components (H_2O) in the calculation is orders of magnitude higher than the solid components, the diagram approximates the T-X_{CO2} diagram as the system is largely dominated by fluid. The results show good agreement with the experimental data from Aranovich and Newton (1999). A more complex calculation for a metapelite in KFMASH is done as a benchmark with the Perple_X and THERMOCALC diagrams and shows good agreement, improving the confidence of the method. Note that in complex systems, it becomes increasingly more demanding to get high resolution phase diagrams. For example a computation with the melt model of Holland et al. (2018) yields a low resolution diagram. Additionally, Cr_2O_3, Fe_2O_3 and K_2O were omitted. However, the topology of the diagram is overall similar. In particular, the melt and pyroxene models used in the reproduction of phase diagram for basalt melting is computationally challenging with the method of linearizing the solutions with discrete hypothetical phase compounds.

5.2 Postprocessing the minimization results

To precompute a lookup table for the local equilibrium the needed unknown variables need to be retrieved from the minimization results. An example is given in Figure 7. The multi-dimensional α array (Line 20, Figure 5) and the corresponding compositions are the only variables that need to be saved along with the P-T arrays.

Using the discrete phase compound linearization approach, mixtures (solid solutions, fluids, melts, gas mixtures) are split into individual phases having a fixed composition. The minimization algorithm will determine which of those discrete phases are stable, and for mixtures this often results in multiple discrete phase compounds with different composition of that mixture being stable. This is a mathematical consequence of solving the optimization program and the thermodynamic meaning is that we have a divariant field in which the composition of mixtures may change. Thermodynamically, it can happen that two or three phases are stable as result of a miscibility gap. However, this needs to be determined by an algorithm that distinguishes the discrete phase compound compositions from each other. If they are significantly different for a given resolution of the discretization, then they are true separate phases. In the other case the properties are obtained from a weighted average into one composition for the true stable phase. Afterwards, only the stable phase amount and the composition are retained. A clustering algorithm is used to determine if we have multiple or single phases stable for each particular mixture (Figure 7, line 10).

To compute the molar volume of each phase we use the numerical derivative of the Gibbs energy:

```
1 clear
2 runname = 'example';
3 load([runname '_linprog']);                                          % load linprog run data
4 molm = molmass_fun(Cname);                                           % get molar mass of the components
5 % Numerics
6 delP     = 1e5;                                                      % for numerical differentiation
7 delc     = 1e-6;
8 solv_tol = 2;                                                        % Tolerance for recognizing exsolved phases
9 % Cluster analysis to find exsolved phases
10 [alph,Npc,p_out,pc_id] = cluster_p(alph,Npc,p,pc_id,solv_tol,phases);    % Compute exsolved, or numerically equivalent phases
11 % For numerical derivatives
12 rho_w         = rho_H2O(T,P,'ZD05');     % Calculate density of water
13 eps_w         = eps_H2O(T,P,rho_w,'S14');% Calculate dielectric constant of water
14 rho_w_dP      = rho_H2O(T,P+delP,'ZD05');% Calculate density of water at P + dP
15 eps_w_dP      = eps_H2O(T,P+delP,rho_w,'S14');% Calculate dielectric constant of water at P + dP
16 [g0,v0]       = tl_g0(T,P,td,rho_w,eps_w); % Calculate endmember Gibbs energies of each solution
17 [g0_dP,v0_dP] = tl_g0(T,P+delP,td,rho_w_dP,eps_w_dP);% Calculate endmember Gibbs energies of each solution at dP
18 g             = tl_gibbs_energy(T,P     ,phases,td,p_out,g0,v0,rho_w,eps_w);            % get Gibbs energy at P
19 g_P           = tl_gibbs_energy(T,P+delP,phases,td,p_out,g0_dP,v0_dP,rho_w_dP,eps_w_dP);% get Gibbs energy at P+dP
20 % Postprocessing
21 Vmol = (g_P-g)/delP;                                                 % Equation 44
22 Mmol = Npc'*molm;                                                    % Equation 45
23 rho  = Mmol./Vmol;                                                   % Equation 46
24 phim = alph/sum(alph);                                               % phi mol
25 phi  = phim.*Vmol./(Vmol'*phim);                                     % Equation 47
26 phiw = phim.*Mmol./(Mmol'*phim);                                     % Equation 48
27 Cwt  = Npc.*repmat(molm,1,size(Npc,2))./repmat(Mmol',size(Npc,1),1);     % Equation 49
28 fluid_id =  strcmp(phases(pc_id),fluid);                             % Find index of fluid
29 solid_id = ~fluid_id;                                                % Find index of solids
30 rhos = rho(solid_id)'*phi(solid_id)/sum(phi(solid_id));               % Equation 50
31 rhof = rho(fluid_id)'*phi(fluid_id)/sum(phi(fluid_id));               % Fluid density
32 % Chemical potentials
33 for iphase = 1:numel(g)
34     Gphase  = g(iphase);
35     mu_last = Gphase;
36     nc      = sum(p_out{pc_id(iphase)}>0);
37     if nc > 1
38         for ic = 1:nc-1
39             c_ind                        = find(p_out{pc_id(iphase)}>0);
40             p1                           = p_out;
41             p1{pc_id(iphase)}(c_ind(ic)) = p_out{pc_id(iphase)}(c_ind(ic)) + delc;
42             p1{pc_id(iphase)}(nc)        = p_out{pc_id(iphase)}(nc) - delc;
43             g_dc                         = tl_gibbs_energy(T,P,phases,td,p1,g0,v0,rho_w,eps_w);
44             Gphase1                      = g_dc(iphase);
45             dGdc1                        = (Gphase1-Gphase)/delc;
46             mu_last                      = mu_last - p_out{pc_id(iphase)}(c_ind(ic)).*dGdc1; % Equation 52
47             mu{iphase}(ic)               = dGdc1;
48         end
49         for ic = 1:nc-1
50             mu{iphase}(ic) = mu{iphase}(ic) + mu_last;                                  % Equation 51
51         end
52     end
53     mu{iphase}(nc) = mu_last;
54 end
55 % Display some results
56 disp(phases(pc_id))                                                    % Display stable phase assemblage
57 disp(phi')                                                            % Display volume fraction
58 disp(Cwt)                                                             % Display phase composition
59 disp(rhos)                                                            % Display solid density
```

Figure 7. *Code example of postprocessing results to prepare a lookup table for use in non-equilibrium processes, such as reactive transport. After loading the result of the minimization in lines 2-3, the molar masses of the components needed in the postprocessing are obtained from an*

external function in line 4. The cluster function in line 10 checks for each stable phase if the phase compounds are numerically distinct to distinguish exsolved phases. Line 12-19 then calculate the densities and dielectric constants and Gibbs energy for the stable phase compositions at P of interest and a small deviation from P of interest for numerical derivatives. Molar volume using a numerical derivative of Gibbs energy is calculated in line 21. Lines 22-31 implement the equations in the text to calculate phase abundances, composition and densities. Line 33-45 calculate the chemical potentials for the components in the phases. From line 56-59 the results are displayed on the screen as an example.

$$V_{mol} = \left(\frac{\partial G}{\partial P} \right)\Big|_T \tag{44}$$

Where the molar mass of each phase is found by:

$$\mathbf{m_{mol}} = \mathbf{molm} \cdot \mathbf{N_{phs}} \tag{45}$$

The density of all phases can then be computed:

$$\boldsymbol{\rho} = \frac{\mathbf{m_{mol}}}{\mathbf{V_{mol}}} \tag{46}$$

Volume fraction ϕ each phase is then found from molar volume and mole fraction obtained from normalizing α to 1 (e.g. $\varphi_{mol} = \alpha / \sum \alpha$):

$$\boldsymbol{\varphi}_{\mathbf{p}} = \frac{\boldsymbol{\varphi}_{\mathbf{mol}} \mathbf{V_{mol}}}{\boldsymbol{\varphi}_{\mathbf{mol}} \cdot \mathbf{V_{mol}}} \tag{47}$$

And weight fraction of each phase:

$$\boldsymbol{\varphi}_{\mathbf{wt}} = \frac{\boldsymbol{\varphi}_{\mathbf{mol}} \mathbf{m_{mol}}}{\boldsymbol{\varphi}_{\mathbf{mol}} \cdot \mathbf{m_{mol}}} \tag{48}$$

Composition in weight is found from:

$$\mathbf{C_{wt}} = \frac{\mathbf{N_{phs}} \mathbf{molm}}{\mathbf{N_{phs}} \cdot \mathbf{molm}} \tag{49}$$

Properties for total rock and fluid can be found from

$$\rho_s = \boldsymbol{\rho}_{\mathbf{ss}} \cdot \boldsymbol{\varphi}_{\mathbf{ss}} \tag{50}$$

Where the vectors hold the densities of all solid minerals including both pure phases and solid solutions, and their volume fractions. Fluid density is simply the density of the fluid mixture from equation and needs no further processing. Total solid concentrations are obtained from summing for each component the weight of all solids and dividing over the total weight.

Chemical potential is calculated following:

$$\mu_i = \mu_{np} + \frac{\partial g}{\partial p_i} \tag{51}$$

Where μ_{np} is the chemical potential of the last dependent proportions (as proportions sum up to 1) and is calculated from:

$$\mu_{np} = g - \sum_{i=1}^{np-1} p_i \frac{\partial g}{\partial p_i} \tag{52}$$

5.3 Improving the calculations

Increasing the resolution of the P-T grid improves the smoothness of the lines in the diagram, but it does not ultimately lead to a better calculation. This is illustrated in Figure 8, where the resolution of the T-X grid for the olivine diagram is kept constant, while the number of discrete compositions for which the olivine and melt are calculated is increased. This means that the mixture is better approximated, and the result is that the compositions and modal abundances become better resolved and the step-like behavior that is present in the calculation with lower compositional grid gradually disappears. Although this is feasible for calculations that involve one or two simple mixtures, like binary olivine and melt, the computational demand required for more complex chemical systems and minerals makes such high-resolution compositional grids unpractical for computation. Even if computers with abundant memory are employed, we found that linprog will not find a solution for systems with more than 2 million discrete phases in the minimization.

Another option to improve the calculation is therefore to refine compositions in an iterative approach as also suggested and employed since decades (Connolly, 2009; Rossi et al., 2009; W. B. White et al., 1958). In Thermolab, this is open for the user to implement or improve. Here we describe a simple approach that currently is employed as a working example. First, an initial minimization is done with a suitable compositional starting grid. This initial starting grid is also subject to possible modification and improvement; however, it is possible to simply set up a coarse resolution initial grid so that each minimization is fast. Each discrete phase which has an alpha above zero is recognized as a stable phase. And the index in the list of non-zero alpha is used to find the composition of the mixture in terms of the endmember proportions and site fractions. In the next step, the proportions are used to generate a denser (i.e., higher resolution) compositional grid around the stable proportions found in the first minimization. For a binary, a simple graphical explanation of this procedure in Thermolab is illustrated in Figure 9. The new higher resolution compositional grid is added to the already existing grid and taken to the next iteration. We checked that the Gibbs energy of the system is always decreasing during the iterations. The iterations are stopped when the Gibbs energy of the system is not changing anymore within limits of machine-precision, or when the compositional spacing in the refined

grid reaches this tolerance. This leads to improved calculation of compositions, modal abundances, as shown in Figure 10 for the metapelite (KFMASH) P-T diagram from Figure 6c.

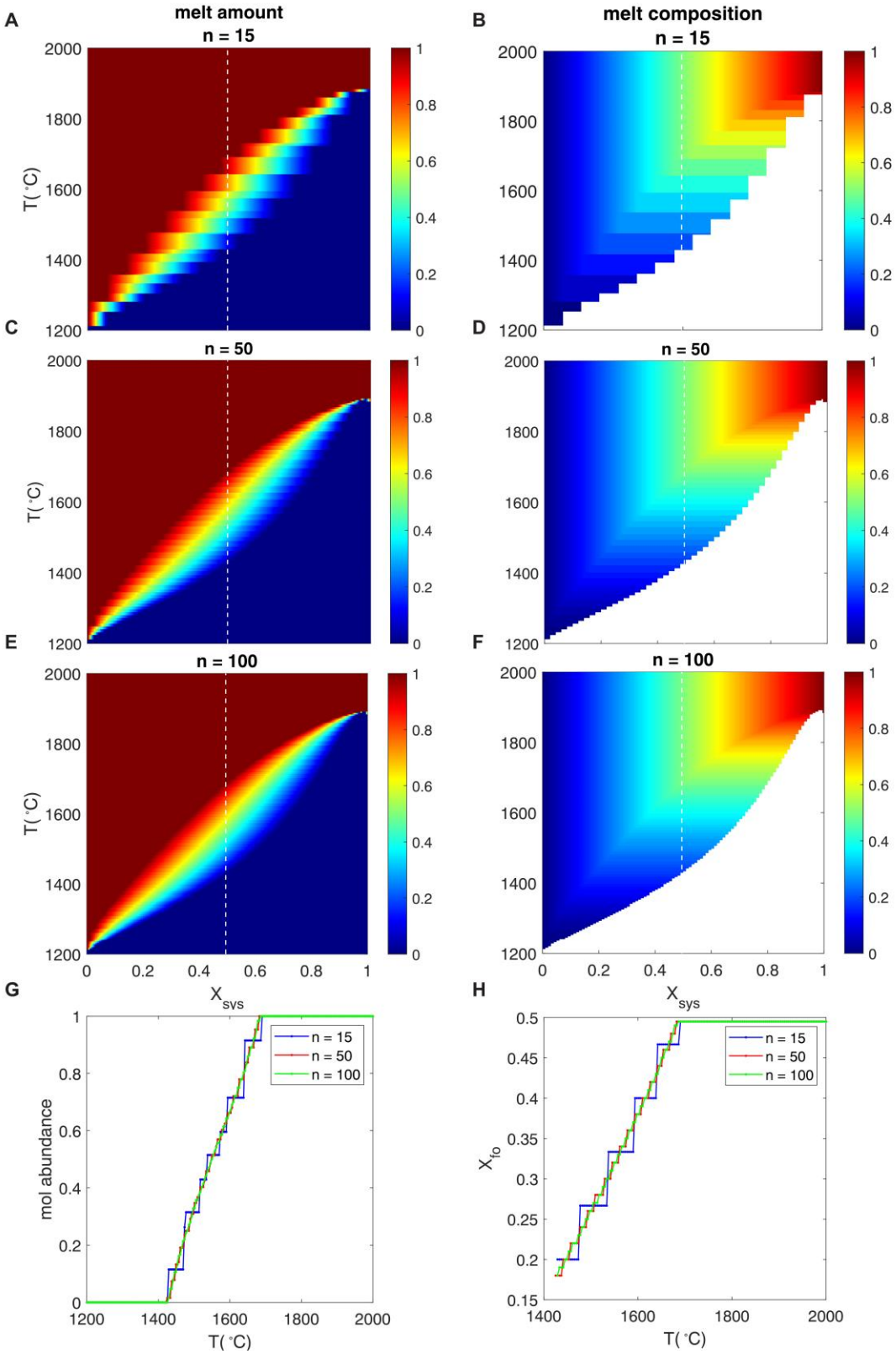

Figure 8 *Influence of resolution of the discretization of solutions on the quality of the thermodynamic calculations. T-X resolution is kept constant at 300x300 steps. By increasing the number of compounds to discretize the mixtures, melt and olivine, the quality of the data is improved and the stepwise behaviour disappears. The melt and olivine binary mixing curves are approximated with 15, 50 and 100 discrete compounds (n).* ***a)*** *Fraction of melt with the melt and solid discretized with 15 compounds.* ***b)*** *Melt composition (X_{fo}) corresponding to (a).* ***c)*** *As in (a), for n = 50 compounds.* ***d)*** *Melt composition corresponding to (c).* ***e)*** *As in (a) with n = 100 compounds.* ***f)*** *Melt composition corresponding to (e).* ***g,h)*** *One-dimensional profiles for melt fraction and composition at X_{sys}=0.5, (dashed lines in a-f). Improvement of calculation with higher number of compounds clearly visible by smoothening of the lines as resolution increases.*

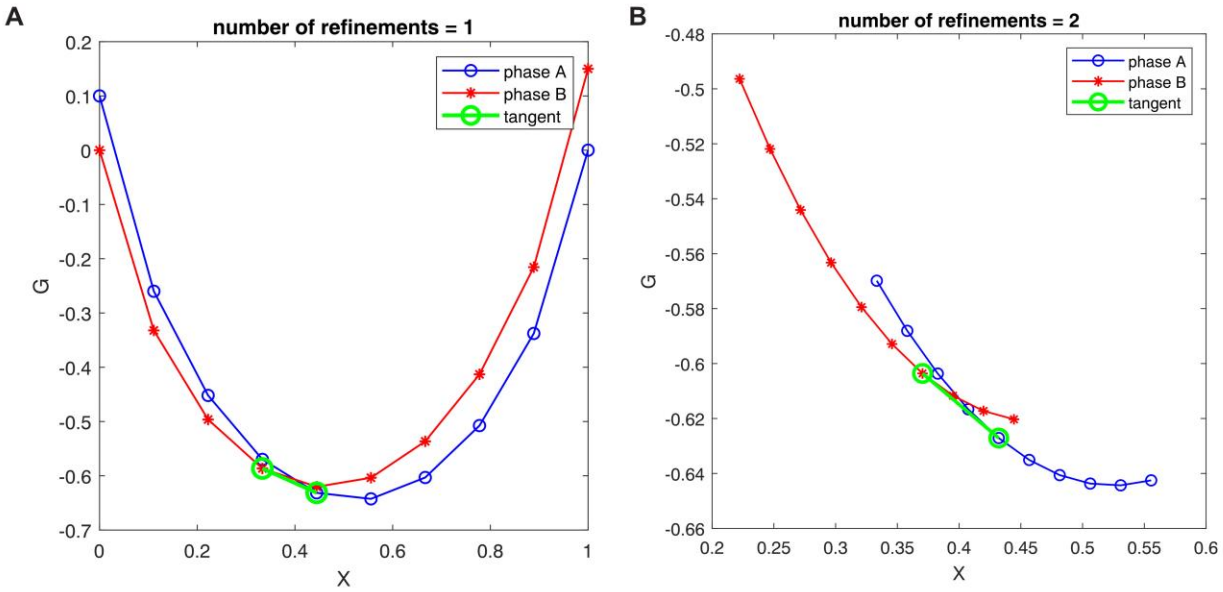

Figure 9. *Conceptual diagrams showing two steps in the refinement of the composition of mixtures.* ***a)*** *Shows an initial minimization result which is then zoomed in and refined around the solution in step one.* ***b)*** *Here the refined compositions are used for a second minimization with smaller compositional spacing between the discretized mixture, without increasing the number of discrete compounds, thereby avoiding using too much computer memory.*

6 Investigating non-linear transport processes in open systems

Coupling local equilibrium thermodynamics to transport processes such as the system of equations introduced above has been discussed previously (e.g. Malvoisin et al., 2015). The method described here follows the approach employed in recent studies of Malvoisin et al, 2015, Plümper et al, 2017, Beinlich et al. 2020). For the transport models a complete set of equilibria for all possible external conditions, T, P, X, may be pre-computed and stored in a lookup table. To this end, loops over P, T, and X can be programmed around the linprog minimization and stored in a database. As an example, we show the soapstone formation in serpentinite from Beinlich et al. (2020). To the initial bulk serpentinite composition carbon (C) is added to produce a lookup table of 150 different bulk compositions at fixed T, and P. Employing the refinement method above, the Beinlich et al (2020), thermodynamic calculations can be improved in smoothness and computation speed (Figure 12b,d,f). However, the main results are the same.

The important aspect is that the Beinlich et al. (2020) calculation was more robust, because no iterative refinement was used and hence any chance of reaching a local-minimum rather than the true minimum was avoided. Thus, the results of Beinlich et al. (2020) serve as benchmark for the refinement algorithm described above.

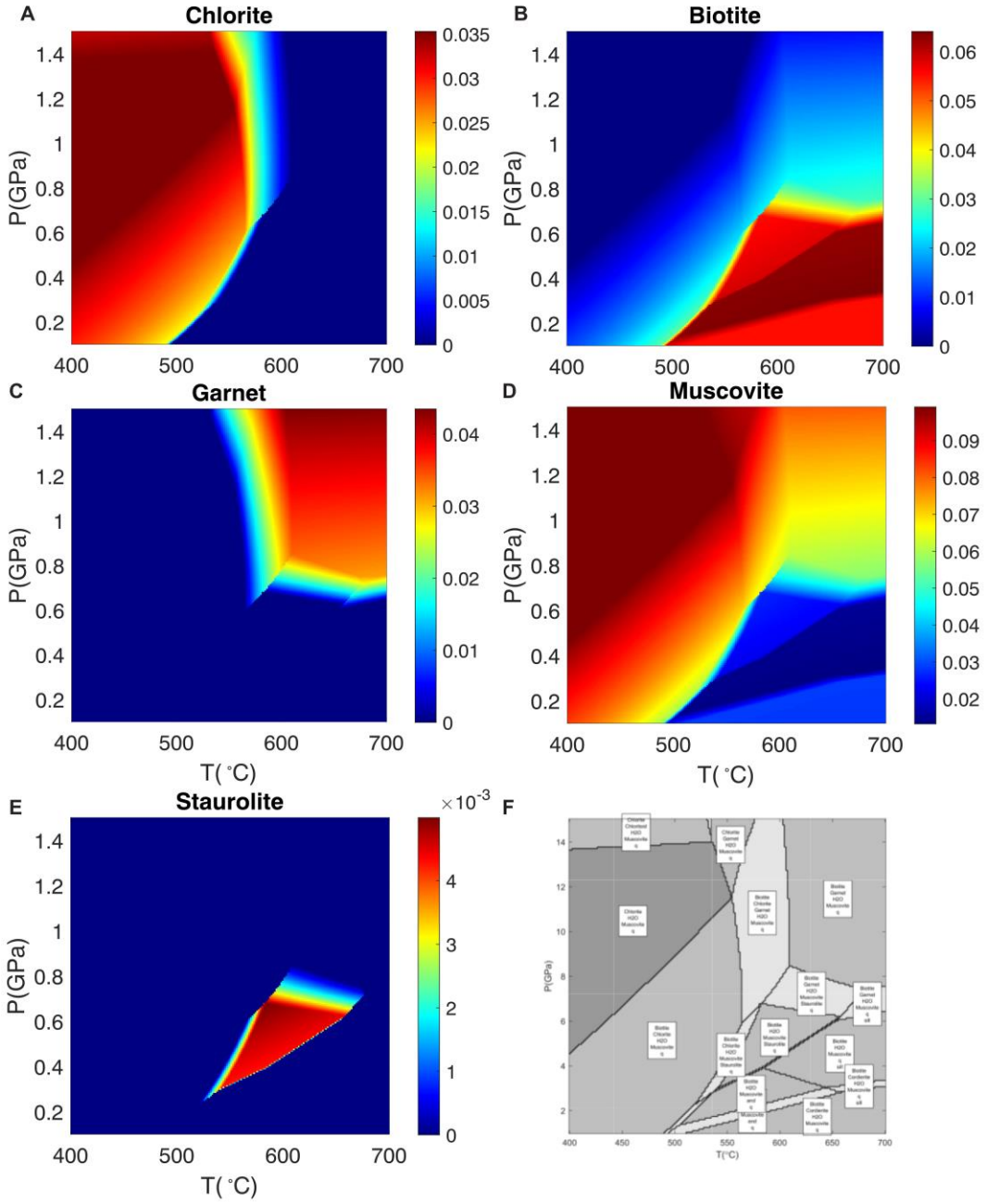

Figure 10. *Example of a phase diagram after refinement. The mineral modes in* ***a)-e)*** *show smooth variations within the phase fields due to sufficiently resolving the compositions of*

*mixtures in a iterative refinement procedure. The final phase diagram in **f)** shows also improvement, but the general topology was also captured in Figure 6c.*

6.1 Reactive transport example

After retrieving the density of solid, fluid, and concentration of fluid and solid, and the chemical potential, the system of equations described above can be solved. Here a possible numerical implementation in MATLAB is shown, using explicit finite differences. The purpose is to focus on the concept of coupling the transport processes to the precomputed local equilibrium lookup table and to show the effect of the non-ideal solution models on reactive transport.

As stated above, there are three equations and 8 unknowns. The first equation is the rearranged total mass balance equation in which the only assumption is that solid is not deforming. The fluid velocities have been substituted by the Darcy flux. This equation is used to find the unknown fluid pressure. The second equation is a mass concentration balance of an immobile component in the solid. This equation can be integrated analytically in case of non-deforming solid and used to calculate the unknown porosity (e. g. Appendix Malvoisin et al. 2015). The last equation is the total mass concentration balance for a component that is mobile, (in Beinlich et al. 2020 this is carbon). From this equation the total mass concentration is found which subsequently can be used to find the solid concentration.

Equation (1) can be written as:

$$\frac{\partial \rho_{tot}}{\partial t} = -\nabla \cdot \left(\rho_f q_D \right) \tag{53}$$

With:

$$\rho_{tot} = \rho_f \phi + \rho_s \left(1 - \phi\right) \tag{54}$$

and (Figure 11, Line 49):

$$q_D = -\frac{k^0 \phi^3}{\mu_f} \nabla P_f \tag{55}$$

When assuming a relation between total density and fluid pressure using an effective compressibility, we can write the above (Figure 11, line 55):

$$\beta_e \frac{\partial P_f}{\partial t} = -\nabla \cdot \left(\rho_f q_D \right) \tag{56}$$

And with the porosity equation (Figure 11, Line 56):

$$\varphi_f = 1 - \frac{\left(1 - \varphi_{f_0}\right) \rho_{s_0} C_{s_0}^{Mg}}{\rho_s C_s^{Mg}} \tag{57}$$

using the concentration of magnesium in solid as immobile species and specifying the initial density, porosity and concentration. Total concentration of mobile species carbon, is solved by rearranging the total mass concentration balance (Figure 11, Line 57):

$$\frac{\partial c_{sys}}{\partial t} = \nabla \bullet \left(\rho_f C_f \varphi D_{C_f} \nabla \mu + \rho_f C_f q_D \right) \tag{58}$$

```
clear,figure(1),clf,colormap(jet)
% Physics
load lookup_soapstone_2021_11_24_n1500_nz15_full
mu_tab   =   mu_tab/max(abs(  mu_tab));
rhos_tab = rhos_tab/max(abs(rhos_tab));
rhof_tab = rhof_tab/max(abs(rhof_tab));
%independent
Lx     = 1;                                                    % Length of model domain (m)
Dc     = 1;                                                    % Diffusion coefficient (m^2/s)
beta   = 1;                                                     % Compressibility, 1/Pa
%nondim
phi0   = 0.2;                                                   % Background porosity (fluid volume fraction)
C0     = 0.004;                                                 % Background CO2 concentration in solid (wt%)
C1     = 0.04715;                                               % Csolid soapstone
npow   = 3;                                                     % Non-linearity in permeability-porosity relation
%dependent
k_muf0 = 1*Dc*beta;                                             % Background permeability/fluid viscosity (m^2/(Pa*s))
P1     = 1e-2/beta;                                             % Boundary fluid pressure (Pa)
t_tot  = 1e+1*Lx^2/Dc;                                          % Total time (s)
% Numerics
nx     = 200;                                                   % Number of grid points in x direction
nt     = 1e9;                                                   % Number of time steps
nout   = 10000;
% preprocessing
dx     = Lx/(nx-1);                                             % Grid step in x
x      = 0:dx:Lx;                                               % X-coordinates of the nodes
% Initialisation;
phi    = x*0 + phi0;                                            % Initial porosity
Pf     = x*0;                                                   % Initial fluid pressure
Cs     = x*0 + C0;                                              % Initial solid concentration
Pf(1)  = P1;                                                    % Left fluid pressure boundary condition
Cs(1)  = C1;                                                    % Left solid CO2 concentration boundary
time   = 0;
% Processing
for it = 1:nt   % Time loop
    mu      = interp1(Cs_tab,mu_tab,Cs);
    Cf      = interp1(Cs_tab,Cf_tab,Cs);                        % Local equilibrium CO2 in fluid from lookup table
    Mg_s    = interp1(Cs_tab,Mg_tab,Cs);                        % Local equilibrium Mg  in solid from lookup table
    rhos    = interp1(Cs_tab,rhos_tab,Cs);                      % Local equilibrium density in solid from lookup table
    rhof    = interp1(Cs_tab,rhof_tab,Cs);                      % Local equilibrium density in fluid from lookup table
    if it == 1,phi_srho_sMg_s0 = (1 - phi).*rhos.*Mg_s;end      % Store initial values
    % averaging
    Crhosys = rhof.*Cf.*phi + rhos.*Cs.*(1-phi);                % Shorthand notation (eq. 54)
    rhofc   = 0.5*(rhof(1:end-1)             + rhof(2:end)          );  % rhof values between the nodes
    rhofCfc = 0.5*(rhof(1:end-1).*Cf(1:end-1) + rhof(2:end).*Cf(2:end));  % rhof*Cf values between the nodes
    phic    = 0.5*( phi(1:end-1)             +  phi(2:end)          );  % phi values between the nodes
    % Fluxes
    qC      = -Dc*rhofCfc.*phic.*diff(mu)/dx;                   % Diffusion flux in fluid (first term in rhs eq. 53)
    qD      =     -k_muf0*phic.^npow.*diff(Pf)/dx;              % Darcy flux (eq. 50)
    % time stepping
    dt_dif = 0.45*dx^2/Dc;                                      % maximum time step of diffusion
    dt_adv = 0.45*dx/max(abs(rhofc.*qD));                       % maximum time step of advection
    dt     = min([dt_adv,dt_dif, t_tot-time]);                  % maximum time step for numerical stability
    % Updates
    phi              = 1 - phi_srho_sMg_s0./(Mg_s.*rhos);       % mass balance of immobile species in solid (eq.52)
    Crhosys(2:end-1) = Crhosys(2:end-1) - dt*(diff(qC + rhofCfc.*qD)/dx); % mass concentration balance of mobile species (eq.54)
    Pf(2:end-1)      = Pf(2:end-1)      - dt*diff(rhofc.*qD)/dx;  % total mass balance (eq.51)
    Cs               = (Crhosys - rhof.*Cf.*phi)./rhos./(1-phi); % calculate new solid concentration (eq. 55)
    time             = time + dt;
    if mod(it,nout)==1 || time == t_tot  %Postprocessing        % plot every nout time step
        phs_modes   = interp1(Cs_tab,vol_frac_solids,Cs);       % find local equilibrium stable phase volume fraction
        area(x,phs_modes,'FaceColor','flat'),axis tight
        legend(solid_names),title(time),drawnow
    end
    if time >= t_tot,break,end
end
```

Figure 11 *Reactive transport code using precomputed equilibrium approach. After loading the precomputed thermodynamic equilibrium data (line 3), the physical parameters are defined in lines 8-19, the numerical parameters (e.g. number of time steps and nodes in the model) are defined (lines 21-23). Preprocessing and initialization including setup of the grid and initial conditions are done in lines 28-33. Here an incoming fluid and fluid pressure increase is setup as left boundary to initialize reactive fluid flow from left to right. In lines 36-40 all properties retrieved from local equilibrium are found by interpolating on the precomputed thermodynamic equilibrium data. Line 41 stores the initial condition for the non-mobile solid and the initial porosity distribution is set to a constant value (phi0 in line 12). Line 43 is the definition of total concentration in the system (Eq.* (59)*). Averaging values used in fluxes defined between the nodes are calculated in line 44-46. Lines 48-49 are the driving forces for the reactive transport, flux of diffusion (qC) and Darcy flux Eq.* (55)*. Adaptive time steps, approximately following Courant Friedrichs-Lewy stability criterium, are calculated in lines 51-53 to constrain numerical error propagation and maintain stability of the numerics. Line 55-57 are most fundamental governing physics in the reactive transport, the main equations* (1), (2), *and* (3)*, by reformulating it to the equations* (56), (57)*, and* (58)*. The solid concentration is found from the definition of total system mass concentration* (59)*). Plotting takes place during model run every 'nout' time steps. The phase abundances can be visualized when desired as they are interpolated from the lookup table and do not enter any of the physics equations. Plotting of the mineralogical evolution is done in lines 61-63.*

With (Figure 11, Line 43):

$$c_{sys} = \rho_f C_f \varphi_f + \rho_s C_s \left(1-\varphi_f\right) \tag{59}$$

Then solid concentration is found by rearranging the above (Figure 11, Line 58):

$$C_s = \frac{c_{sys} - \rho_f C_f \varphi_f}{\rho_s \left(1-\varphi_f\right)} \tag{60}$$

The remaining unknowns, ρ_f, ρ_s ,C_{sMg}, and C_f are found from interpolation in the lookup table at each time step (Figure 11, Line 36-40). Details of the coding example are found in the caption of Figure 11 and results of the transport code are shown in Figure 12. The non-linearity of the thermodynamic relationship between solid and fluid composition is demonstrated in Figure (12,c,d,f), this is a result of both the non-ideality of solution models as well as changes in the phase assemblage. Depending on the function of solid composition versus fluid composition, the reaction fronts behave very differently in terms of shape and velocity (Figure 12, a, c,e).

6.2 Cahn-Hilliard exsolution

Natural processes usually are not in equilibrium and do not strictly follow the path that can be followed from a phase diagram. Instead, there will be a process that develops towards the state of global equilibrium depicted on a phase diagram although it may never reach it (e.g. due to thermal closure). With Thermolab, the Gibbs energies can be directly used instead of first calculating thermodynamic equilibrium and the process towards equilibrium can be modelled. A demonstration of this is given by solving the Cahn-Hilliard equations in which driving force for

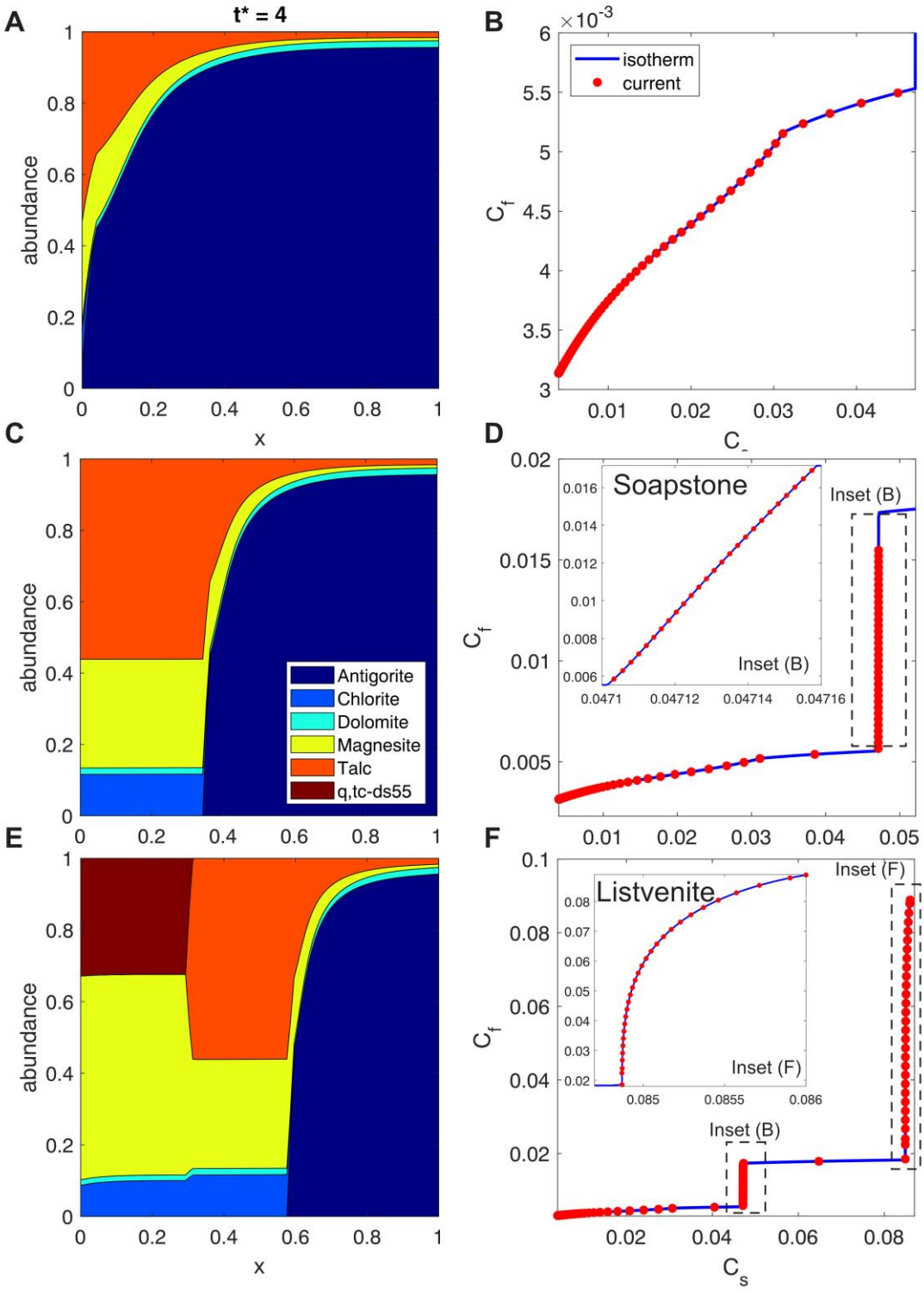

Figure 12. *Snapshot of reaction fronts produced by influx of three different incoming CO_2 fluid compositions from the left boundary into a serpentinite using the code in Figure 11. For comparison all runs were stopped after the same duration. In all cases, the starting rock consists primarily of serpentine (here antigorite), with minor amounts of talc, magnesite and dolomite.* ***a)*** *If the incoming fluid composition lies below ~0.005 antigorite never completely disappears and a*

gradual reaction front forms transforming the serpentinite to ophimagnesite (magnesite-talc-serpentinite). ***b)*** *The equilibrium relation between C_f and C_s (i.e. the isotherm) shown in blue with the transient (current) C_f and C_s compositions plotted as red dots.* ***c)*** *With an incoming fluid composition between 0.01-0.015, the pristine serpentinite to the right transforms into soapstone with a sharp reaction front when antigorite has reacted out.* ***d)*** *The equilibrium relation between C_f and C_s (i.e. the isotherm). The steep slope at C_s between ~0.045-0.052 is enlarged in the inset. Here antigorite disappears (the soapstone on the left in Figure c), and the steepness of the slope on the isotherm causes a sharp soapstone front. The shallow slopes below C_s=0.045 correspond to the transitional front where serpenitinite is partially transformed to soapstone.* ***e)*** *Development of an additional reaction front, forming listvenite (quartz-magnesite rock), as incoming fluid composition is now higher, ~ 0.086 weight fraction dissolved carbon.* ***f)*** *As the incoming fluid composition lies on anorther steep part of the isotherm, the listvenite front is also sharp. Inset shows the curvature of the isotherm corresponding to the listvenite stable assemblage. Endmember data from the tc-ds55 dataset (Holland & Powell, 1998), solution models: CO_2-H_2O Fluid (Aranovich & Newton, 1999), Antigorite (Padron-Navarta et al., 2013), Chlorite (Holland et al., 1998), Talc (Holland & Powell, 1998), Magnesite, Dolomite (R. W. White et al., 2003). t* = dimensionless time. Concentration units are in elemental carbon weight fraction.*

diffusion is chemical potential and an uphill diffusion process causes an initial random homogeneous system to develop into an equilibrium phase assemblage (Cahn & Hilliard, 1958). A simplified version of the Cahn-Hilliard equation consists of a balance of mass concentration and a flux equation for the diffusion. Assuming a system without fluid, and assuming constant densities a basic mass concentration balance can be written (Figure 13, line 35):

$$\frac{\partial C_{s,1}}{\partial t} = -\frac{\partial q_{c_{s,1}}}{\partial x} \tag{61}$$

Flux of concentration in solid of a component can be defined as a function of gradients in chemical potential differences or a single chemical potential in conjuction with the Gibbs-Duhem relation (e.g. p. 80 in Lebon et al., 2008; Nauman & He, 2001), here the former is used (Figure 13, line 34):

$$q_{c_{s,1}} = -D_{c_{s,1}} C_{s,1} \frac{\partial\left(\mu_{C_{s,1}} - \mu_{C_{s,2}}\right)}{\partial x} \tag{62}$$

The chemical potential difference can be conveniently expressed by:

$$\mu_{C_{s,1}} - \mu_{C_{s,2}} = \frac{\partial g_{mix}}{\partial C_{s,1}} - \gamma \frac{\partial^2 C_{s,1}}{\partial x^2} \tag{63}$$

where the last term in (63) is the interfacial free energy contribution as introduced by Cahn-Hilliard (1958). Similar to Figure 7, the chemical potential can be calculated with numerical differentiation of the Gibbs energy (see Figure 13, line 31-32).

These equations describe the spinodal decomposition of a phase with strong non-ideal behaviour, such as feldspar, due to non-linear diffusion driven by chemical potential gradients. A useful review is found in Nauman & He (2001). See also caption Figure 14 for details.

```
1 clear,clf
2 % Physics
3 Lx = 1;                                                  % Model domain length
4 Dc = 1;                                                  % Diffusion coefficient
5 % Thermodynamics
6 T        = 500 + 273.15;                                 % Temperature (K)
7 P        = 1e8;                                          % Pressure (Pa)
8 phs_name = {'Feldspar(C1)'};                             % phase name
9 Cname    = {'Si','Al','Na','K','O'};                     % system components
10 td       = init_thermo(phs_name,Cname,'solution_models_H18');  % load static thermodynamic data
11 [g0,V0]  = tl_g0(T,P,td);                                % get endmember gibbs energies of the solution model
12 % Numerics
13 nx   = 500;                                             % Grid resolution
14 nt   = 1e10;                                            % number of time steps
15 nout = 5000;                                            % plotting each nout time step
16 gam  = 1e-1;                                            % Cahn Hilliard surface energy parameter
17 delC = 1e-3;                                            % delta concentration for numerical derivative
18 % Preprocessing
19 dx = Lx/(nx-1);                                         % grid step
20 dt = min(dx^2/Dc/2.1,dx^4/gam/16.1);                    % time step
21 x  = 0:dx:Lx;                                           % x coordinates
22 % Initialization
23 c    = 0.5 + 0.01*rand(1,nx);                           % initial concentration of albite
24 cini = c;                                               % store initial concentration for plot
25 % Processing
26 for it = 1:nt
27     p{1}        = [c; 1-c]';                            % proportions of endmembers Ab-Or
28     p_dC{1}     = [c+delC; 1-(c+delC)]';                % proportions of endmembers Ab-Or plus delta C
29     g_p         = tl_gibbs_energy(T,P,phs_name,td,p_dC,g0,V0); % Gibbs energy + delta G, for numerical derivative
30     g           = tl_gibbs_energy(T,P,phs_name,td,p   ,g0,V0); % Gibbs energy
31     mu          = (g_p-g)'/delC;                        % mu1 - mu2; numerical derivative dg/dc
32     mu(2:end-1) = mu(2:end-1) - gam*diff(c,2)/dx^2;     % Cahn-Hilliard (1958)
33     cc          = (c(1:end-1)+c(2:end))/2;              % Centered concentrations between gridpoints
34     qc          = -Dc*cc.*diff(mu)/dx;                  % Non-Fickean Diffusion flux
35     c(2:end-1)  = c(2:end-1) - dt*diff(qc)/dx;          % Concentration balance with assumptions
36     c(1:3)      = mean(c(1:3));                         % no flux left boundary
37     c(end-2:end)= mean(c(end-2:end));                   % no flux right boundary
38     % Postprocessing
39     if mod(it,nout) == 1
40         plot(x,c,x,cini),title(mean(c)),axis([0 1 0 1])      % plot concentration versus distance
41         drawnow
42     end
43 end
```

Figure 13 *Cahn-Hilliard example code for 1D binary exsolution. The length of the domain and diffusion coefficient, assumed constant for simplicity here, are defined in line 3-4, after which the thermodynamic data is loaded for a given P-T. The phase for which Gibbs energy is calculated is input in line 8, and the components in the system can be given in line 9. Line 10 initializes static thermodynamic data as in Figure 5. Line 11 calculates the Gibbs energy of the endmembers in the solution (this is done to increase performance as they do not vary here). Numerical parameters are setup in lines 13-17, followed by preprocessing for generating the grid and the time step. An initial setup consists of a homogeneous concentration with small random perturbations. The physical process is modelled in a time loop from line 26-43. Line 27-30 shows how Thermolab is used without precomputed lookup tables. A small increment of proportions of*

the endmembers is used to make a numerical derivative to calculate the chemical potential in line 31, with Cahn-Hilliard addition of energy regularization (line 32). The chemical potential gradients drive diffusion in the system via the diffusion flux in line 34 and line 35 is the mass concentration balance in simplified form. Line 36-37 are boundary conditions that ensure total concentration in the system remains constant. Line 39-42 are plotting the results as the model runs.

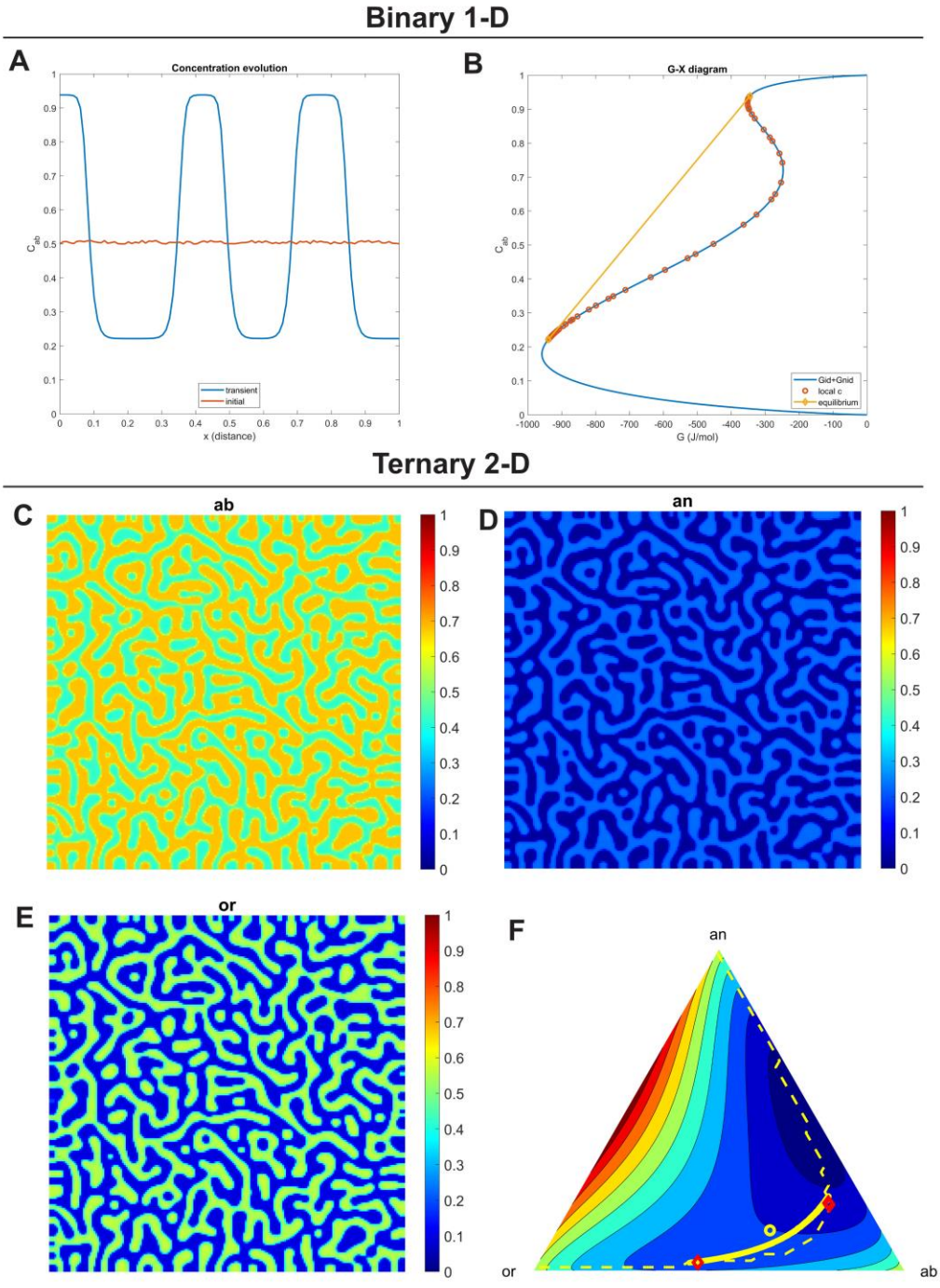

Figure 14 *Example of using Thermolab without precomputed thermodynamic data. Physical processes develop towards thermodynamic equilibrium using the Cahn-Hilliard model at 500 °C, 0.1 GPa. The 1D example code for a binary system is given in Figure 13. An initially homogenous concentration distribution in a single phase develops into a two phase system due to uphill diffusion as a result of the non-linearity of solution models (the non-ideality that leads to exsolution of phases).* ***a)*** *Snapshot of a 1D model during exsolution of binary feldspar (concentration corresponds to albite component in albite-sanidine mixture). Red line shows initial concentration distribution developing into separate phases represented by the blue line.* ***b)*** *Comparing the concentrations in the physical domain to the Gibbs energy-composition (X) curve (for clarity only the mixing energy, ideal + non-ideal is shown). Plotting the transient concentrations on the equilibrium curve shows that the system develops towards the tangent construction (i.e. equilibrium condition) shown with the yellow line and calculated with 'linprog' following methods described in the main text.* ***c)*** *Albite concentration in a 2D feldspar model after exsolving for some time from a homogeneous initial distribution.* ***d)****, and* ***e)*** *represent the corresponding compositions of respectively, components anorthite, orthoclase (using sanidine endmember here).* ***f)*** *transient compositions of the feldspar for all nodes in the 2D domain plotted on the equilibrium mixing Gibbs-energy ternary represented by the contours. These compositions form a continuous yellow line (as there are many overlapping symbols). Dashed line corresponds to solvus computed with 'linprog', and yellow open circle corresponds to average concentration in the system. Red symbols are equilibrium compositions of the two stable phases from Gibbs minimization.*

7 Discussion

The motivation befind the development of Thermolab is to study the effects of the non-ideality of solution models in reactive transport processes in open systems. Most natural materials including minerals, rocks, melt, fluids and gases display some degree of non-ideal mixing behaviour (e.g. Ganguly, 2020). We showed that for the case study of the soapstone formation studied by Beinlich et al. (2020) both the shape and the velocity of the reaction front vary strongly depending on the non-linearity of the partitioning of carbon between fluid and solid (Figure 12). For evaluating potential risks during transport of nuclear waste material understanding this non-linear behaviour is crucial and a study of Shao et al. (2009) is line with this conclusion.

For mathematical analysis the formulation of complex solution models is important to show in a transparent manner such that non-linearities in transport processes can be studied. Therefore we presented the linear algebraic approach that is used in Thermolab to compute Gibbs energy of mixing for arbitrary multi-component phases (Figure 1). The starting point was a crystallographic or structural model of a solution and a predefined set of endmembers as developed by previous workers (e.g. Green et al., 2016; Palin et al., 2016). More in depth discussion on how to newly define crystallographic and speciation models for solid solutions is given by Myhill & Connolly (2021), after which the model should then be fitted to experimental data.

Complex solution models are almost exclusively used for phase diagram calculations (e.g. Connolly, 2005, 2009; de Capitani & Brown, 1987; Ghiorso et al., 2002; Holland & Powell, 1998, 2011; Johnson et al., 1992), but usually not for the transport codes. To ensure the reliability of the Gibbs energy calculation and equilibrium calculation methods, Thermolab is

benchmarked versus phase diagrams and exemplified in use for reactive transport projects. Constrained Gibbs energy minimization is discussed following existing approaches (Connolly, 2005; W. B. White et al., 1958) and the results are then used to calculate equilibrium compositions and retrieve the so-called isotherm that can be used in a transport code.

The isotherm, introduced in chromatographic studies of metasomatism, is a relation between fluid and solid composition at fixed P-T (Hofmann, 1972). An approach in which the system is divided in solid and fluid and for which the mass conservations equations have been summed up to eliminate reaction source terms has proven very useful for reaction front propagation studies (Orr, 2005). Shape and velocity of propagating reaction fronts strongly depend on the non-linearity of solutions models (Guy, 1993). The approach of pre-computing the equilibrium compositions and using the results as an isotherm in the transport codes is useful to study the effects of the non-linearity of solution models on reactive transport. As the studies of Hofmann (1972) and Guy (1993) focus on single phases, our results shows this is functioning similarly on multi-phase systems such as rocks. The steep reaction fronts act similar to isotherms with miscibility gaps (Fletcher & Hofmann, 1974), but the solid solutions are responsible for the continuity of the isotherm across the 'jump-like' curves. Previous studies usually introduced simple isotherms, also called flow functions, to study the behaviour during transport. Thermolab has been motivated by the need to generate realistic flow functions using complex solution models.

Solid solutions with strong non-ideal behaviour result in phase separation due to non-linear diffusion when combined with transport models. The Cahn-Hilliard model (Cahn & Hilliard, 1958) is used to stabilize the numerical solutions by introducing an energy penalty for generating surfaces between phases introduced by a surface energy parameter. This method is widely applied in material science (Nauman & He, 2001) and also some geological appliciations have been studied (Abart et al., 2009; Petrishcheva & Abart, 2009). For geological materials other than feldspar, the behaviour of such non-linear diffusion systems can be further investigated with Thermolab.

Mixing of databases is possible in a flexible framework like Thermolab, however it may not be recommended since internally consistent databases are not necessarily consistent amongst each other. Nevertheless, to use aqueous species in fluids together with most up to date solution models of minerals, the only possibility to date is to combine for example SUPCRT databases with Holland and Powell (1998, 2011). It has been argued that such a combination may serve as a good approximation (Dolejš, 2013), when appropriate equations of state and dielectric constant for water are used. However, refitting the aqueous species databases from SUPCRT in conjunction with mineral database of Holland and Powell (1998) is likely the more reliable approach to combine datasets (Miron et al., 2016; Miron et al., 2017).

8 Conclusions

With thermolab it is possible to reproduce published phase diagrams involving complex solution models and these solution models can then be used in transport codes to investigate the effects of non-linearity on the open system processes. Complex flow functions can be retrieved from Thermolab and used in mathematical analysis and numerical models of reactive transport. Gibbs energy can be directly used to construct chemical potentials as driving force for non-linear diffions leading to phase separation.

The modelling framework provided by Thermolab allows users to add custom functions, include new databases, design solution models but also improve procedures to calculate equilibrium. Limits of the discretization of solutions approach are due to computer memory restrictions, which for complex solution models increases computation time to unpractical durations. Computers with increased memory would be a solution, however, we found that the linprog algorithm will stop to converge when about 2 million discrete phases or more in systems with more than six components are used. Refinement strategies are a potential solution to this problem; however, these compromise the robustness of the result by possibly missing the global minimum of the Gibbs energy. Thus, Thermolab leaves the door open for development of faster and more robust future algorithms by a transparent open source coding environment, which due to the compactness of MATLAB example code can be translated to other programming languages with minimum effort.

Acknowledgments

"The Deutsche Forschungsgemeinschaft (DFG) financially supported this research for Johannes C. Vrijmoed through grant CRC 1114 'Scaling Cascades in Complex Systems', Project Number 235221301, Project (C09) – 'Dynamics of rock dehydration on multiple scales'." Yuri Y. Podladchikov was supported by the Russian Ministry of Science and Higher Education (project no. 075-15-2019-1890). There were no financial or affiliation conflicts of interest for the authors.

Open Research

Thermolab is made available at https://hansjcv.github.io/Thermolab/. These pages may be subject to continuous update and development.

References

Abart, R., Petrishcheva, E., Wirth, R., & Rhede, D. (2009). Exsolution by Spinodal Decomposition Ii: Perthite Formation during Slow Cooling of Anatexites from Ngoronghoro, Tanzania. *American Journal of Science, 309*(6), 450-475.

Ague, J. J., & Baxter, E. F. (2007). Brief thermal pulses during mountain building recorded by Sr diffusion in apatite and multicomponent diffusion in garnet. *Earth and Planetary Science Letters, 261*(3-4), 500-516.

Aharonov, E., Whitehead, J. A., Kelemen, P. B., & Spiegelman, M. (1995). Channeling Instability of Upwelling Melt in the Mantle. *Journal of Geophysical Research-Solid Earth, 100*(B10), 20433-20450.

Anderson, G. M., Castet, S., Schott, J., & Mesmer, R. E. (1991). The Density Model for Estimation of Thermodynamic Parameters of Reactions at High-Temperatures and Pressures. *Geochimica Et Cosmochimica Acta, 55*(7), 1769-1779.

Aranovich, L. Y., Akinfiev, N. N., & Golunova, M. (2020). Quartz solubility in sodium carbonate solutions at high pressure and temperature. *Chemical Geology, 550*.

Aranovich, L. Y., & Newton, R. C. (1999). Experimental determination of CO2-H2O activity-composition relations at 600-1000 degrees C and 6-14 kbar by reversed decarbonation and dehydration reactions. *American Mineralogist, 84*(9), 1319-1332.

Balashov, V. N., & Yardley, B. W. D. (1998). Modeling metamorphic fluid flow with reaction-compaction-permeability feedbacks. *American Journal of Science, 298*(6), 441-470.

Bebout, G. E., Scholl, D. W., Stern, R. J., Wallace, L. M., & Agard, P. (2018). Twenty Years of Subduction Zone Science: Subduction Top to Bottom 2 (ST2B-2). *GSA Today*, 4-10.

Beinlich, A., John, T., Vrijmoed, J. C., Tominaga, M., Magna, T., & Podladchikov, Y. Y. (2020). Instantaneous rock transformations in the deep crust driven by reactive fluid flow. *Nature Geoscience, 13*(4), 307-311.

Berman, R. G. (1988). Internally-Consistent Thermodynamic Data for Minerals in the System Na2o-K2o-Cao-Mgo-Feo-Fe2o3-Al2o3-Sio2-Tio2-H2o-Co2. *Journal of Petrology, 29*(2), 445-522.

Berman, R. G., & Brown, T. H. (1985). Heat-Capacity of Minerals in the System Na2o-K2o-Cao-Mgo-Feo-Fe2o3-Al2o3-Sio2-Tio2-H2o-Co2 - Representation, Estimation, and High-Temperature Extrapolation. *Contributions to Mineralogy and Petrology, 89*(2-3), 168-183.

Bowen, N. L., & Schairer, J. F. (1935). The system MgO-FeO-SiO2. *American Journal of Science, s5-29*(170), 151-217.

Cahn, J. W., & Hilliard, J. E. (1958). Free Energy of a Nonuniform System .1. Interfacial Free Energy. *Journal of Chemical Physics, 28*(2), 258-267.

Coggon, R., & Holland, T. J. B. (2002). Mixing properties of phengitic micas and revised garnet-phengite thermobarometers. *Journal of Metamorphic Geology, 20*(7), 683-696.

Connolly, J. A. D. (2005). Computation of phase equilibria by linear programming: A tool for geodynamic modeling and its application to subduction zone decarbonation. *Earth and Planetary Science Letters, 236*(1-2), 524-541.

Connolly, J. A. D. (2009). The geodynamic equation of state: What and how. *Geochemistry Geophysics Geosystems, 10*.

Connolly, J. A. D. (2017). A Primer in Gibbs Energy Minimization for Geophysicists. *Petrology, 25*(5), 526-534.

Dantzig, G. B., Orden, A., & Wolfe, P. (1955). The generalized simplex method for minimizing a linear form under linear inequality restraints. *Pacific Journal of Math, 5*, 183-195.

de Capitani, C., & Brown, T. H. (1987). The computation of chemical equilibrium in complex systems containing non-ideal solutions. *Geochimica Et Cosmochimica Acta, 51*(10), 2639-2652.

De Groot, S., & Mazur, P. (1984). *Non-equilibrium thermodynamics*. New York: Dover Publications, Inc.

Dolejš, D. (2013). Thermodynamics of Aqueous Species at High Temperatures and Pressures: Equations of State and Transport Theory. *Reviews in Mineralogy and Geochemistry, 76*(1), 35-79.

Dolejš, D., & Wagner, T. (2008). Thermodynamic modeling of non-ideal mineral–fluid equilibria in the system Si–Al–Fe–Mg–Ca–Na–K–H–O–Cl at elevated temperatures and pressures: Implications for hydrothermal mass transfer in granitic rocks. *Geochimica Et Cosmochimica Acta, 72*(2), 526-553.

Evans, K. A., & Powell, R. (2006). Improvements in thermodynamic models of hydrothermal fluids through better configurational entropy terms. *Geochimica Et Cosmochimica Acta, 70*(18), A162-A162.

Evans, K. A., & Powell, R. (2007). DES-code: A metacode to aid calculation of the chemical potential of aqueous solutions at elevated temperatures and pressures. *Computers & Geosciences, 33*(6), 789-807.

Fagents, S. A., Gregg, T. K. P., & Lopes, R. M. C. (2013). *Modeling Volcanic Processes*.

Feng, G., Wang, Y., Xu, T., Wang, F., & Shi, Y. (2021). Multiphase flow modeling and energy extraction performance for supercritical geothermal systems. *Renewable Energy, 173*, 442-454.

Fernández, D. P., Goodwin, A. R. H., Lemmon, E. W., Levelt Sengers, J. M. H., & Williams, R. C. (1997). A Formulation for the Static Permittivity of Water and Steam at Temperatures from 238 K to 873 K at Pressures up to 1200 MPa, Including Derivatives and Debye–Hückel Coefficients. *Journal of Physical and Chemical Reference Data, 26*(4), 1125-1166.

Fletcher, R. C., & Hofmann, A. W. (1974). Simple models of diffusion and combined diffusion-infiltration metasomatism. *Geochemical Transport and Kinetics*, 243-259.

Ganguly, J. (2020). *Thermodynamics in Earth and Planetary Sciences / by Jibamitra Ganguly* (2nd ed. 2020 ed.). Cham: Springer International Publishing.

Geller, R. J. (1997). Earthquake prediction: a critical review. *Geophysical Journal International, 131*(3), 425-450.

Ghiorso, M. S., Hirschmann, M. M., Reiners, P. W., & Kress, V. C. (2002). The pMELTS: A revision of MELTS for improved calculation of phase relations and major element partitioning related to partial melting of the mantle to 3 GPa. *Geochemistry, Geophysics, Geosystems, 3*(5), 1-35.

Glasser, F. P., Jauffret, G., Morrison, J., Galvez-Martos, J.-L., Patterson, N., & Imbabi, M. S.-E. (2016). Sequestering CO2 by Mineralization into Useful Nesquehonite-Based Products. *Frontiers in Energy Research, 4*.

Gordon, S., & McBride, B. J. (1994). Computer Program for the Calculation of Complex Chemical Equilibrium Compositions with Applications; I. Analysis. *NASA Reference Publication, 1311*.

Green, E. C. R., White, R. W., Diener, J. F. A., Powell, R., Holland, T. J. B., & Palin, R. M. (2016). Activity-composition relations for the calculation of partial melting equilibria in metabasic rocks. *Journal of Metamorphic Geology, 34*(9), 845-869.

Guy, B. (1993). Mathematical revision of Korzhinskii's theory of infiltration metasomatic zoning. *European Journal of Mineralogy, 5*(2), 317-340.

Helgeson, H. C., Delany, J. M., Nesbitt, H. W., & Bird, D. K. (1978). Summary and Critique of the Thermodynamic Properties of Rock-Forming Minerals. *American Journal of Science, 278*, 1-229.

Helgeson, H. C., Kirkham, D. H., & Flowers, G. C. (1981). Theoretical Prediction of the Thermodynamic Behavior of Aqueous-Electrolytes at High-Pressures and Temperatures .4. Calculation of Activity-Coefficients, Osmotic Coefficients, and Apparent Molal and Standard and Relative Partial Molal Properties to 600-Degrees-C and 5 Kb. *American Journal of Science, 281*(10), 1249-1516.

Hofmann, A. (1972). Chromatographic theory of infiltration metasomatism and its application to feldspars. *American Journal of Science, 272*(1), 69-90.

Holland, T. J. B., Baker, J., & Powell, R. (1998). Mixing properties and activity-composition relationships of chlorites in the system MgO-FeO-Al2O3-SiO2-H2O. *European Journal of Mineralogy, 10*(3), 395-406.

Holland, T. J. B., Green, E. C. R., & Powell, R. (2018). Melting of Peridotites through to Granites: A Simple Thermodynamic Model in the System KNCFMASHTOCr. *Journal of Petrology, 59*(5), 881-899.

Holland, T. J. B., & Powell, R. (1991). A Compensated-Redlich-Kwong (Cork) Equation for Volumes and Fugacities of Co2 and H2o in the Range 1-Bar to 50-Kbar and 100-1600-Degrees-C. *Contributions to Mineralogy and Petrology, 109*(2), 265-273.

Holland, T. J. B., & Powell, R. (1996). Thermodynamics of order-disorder in minerals .1. Symmetric formalism applied to minerals of fixed composition. *American Mineralogist, 81*(11-12), 1413-1424.

Holland, T. J. B., & Powell, R. (1998). An internally consistent thermodynamic data set for phases of petrological interest. *Journal of Metamorphic Geology, 16*(3), 309-343.

Holland, T. J. B., & Powell, R. (2003). Activity-composition relations for phases in petrological calculations: an asymmetric multicomponent formulation. *Contributions to Mineralogy and Petrology, 145*(4), 492-501.

Holland, T. J. B., & Powell, R. (2011). An improved and extended internally consistent thermodynamic dataset for phases of petrological interest, involving a new equation of state for solids. *Journal of Metamorphic Geology, 29*(3), 333-383.

Huang, F., & Sverjensky, D. A. (2019). Extended Deep Earth Water Model for predicting major element mantle metasomatism. *Geochimica Et Cosmochimica Acta, 254*, 192-230.

John, T., Gussone, N., Podladchikov, Y. Y., Bebout, G. E., Dohmen, R., Halama, R., et al. (2012). Volcanic arcs fed by rapid pulsed fluid flow through subducting slabs. *Nature Geoscience, 5*(7), 489-492.

Johnson, J. W., & Norton, D. (1991). Critical Phenomena in Hydrothermal Systems - State, Thermodynamic, Electrostatic, and Transport-Properties of H2o in the Critical Region. *American Journal of Science, 291*(6), 541-648.

Johnson, J. W., Oelkers, E. H., & Helgeson, H. C. (1992). Supcrt92 - a Software Package for Calculating the Standard Molal Thermodynamic Properties of Minerals, Gases, Aqueous Species, and Reactions from 1-Bar to 5000-Bar and 0-Degrees-C to 1000-Degrees-C. *Computers & Geosciences, 18*(7), 899-947.

Kelemen, P. B., & Matter, J. (2008). In situ carbonation of peridotite for CO2 storage. *Proceedings of the National Academy of Sciences, 105*(45), 17295-17300.

Kulik, D. A., Wagner, T., Dmytrieva, S. V., Kosakowski, G., Hingerl, F. F., Chudnenko, K. V., & Berner, U. R. (2012). GEM-Selektor geochemical modeling package: revised algorithm and GEMS3K numerical kernel for coupled simulation codes. *Computational Geosciences*.

Lebon, G., Jou, D., & Casas-Vázquez, J. (2008). *Understanding non-equilibrium thermodynamics : foundations, applications, frontiers / G. Lebon, D. Jou, J. Casas-Vázquez*. Berlin ; Heidelberg: Springer.

Lichtner, P. C., & Carey, J. W. (2006). Incorporating solid solutions in reactive transport equations using a kinetic discrete-composition approach. *Geochimica Et Cosmochimica Acta, 70*(6), 1356-1378.

Malvoisin, B., Podladchikov, Y. Y., & Vrijmoed, J. C. (2015). Coupling changes in densities and porosity to fluid pressure variations in reactive porous fluid flow: Local thermodynamic equilibrium. *Geochemistry Geophysics Geosystems, 16*(12), 4362-4387.

Manning, C. E. (1994). The Solubility of Quartz in H_2O in the Lower Crust and Upper-Mantle. *Geochimica Et Cosmochimica Acta, 58*(22), 4831-4839.

Miron, G. D., Wagner, T., Kulik, D. A., & Heinrich, C. A. (2016). Internally consistent thermodynamic data for aqueous species in the system Na-K-Al-Si-O-H-Cl. *Geochimica Et Cosmochimica Acta, 187*, 41-78.

Miron, G. D., Wagner, T., Kulik, D. A., & Lothenbach, B. (2017). An internally consistent thermodynamic dataset for aqueous species in the system Ca-Mg-Na-K-Al-Si-O-H-C-Cl TO 800 degrees C AND 5 kbar. *American Journal of Science, 317*(7), 755-806.

Nauman, E. B., & He, D. Q. (2001). Nonlinear diffusion and phase separation. *Chemical Engineering Science, 56*(6), 1999-2018.

Orr, F. M. (2005). *Theory of Gas Injection Processes*. Stanford, California: Stanford University.

Orr, F. M. (2018). Carbon Capture, Utilization, and Storage: An Update. *Spe Journal, 23*(06), 2444-2455.

Padron-Navarta, J. A., Sanchez-Vizcaino, V. L., Hermann, J., Connolly, J. A. D., Garrido, C. J., Gomez-Pugnaire, M. T., & Marchesi, C. (2013). Tschermak's substitution in antigorite and consequences for phase relations and water liberation in high-grade serpentinites. *Lithos, 178*, 186-196.

Palin, R. M., White, R. W., Green, E. C. R., Diener, J. F. A., Powell, R., & Holland, T. J. B. (2016). High-grade metamorphism and partial melting of basic and intermediate rocks. *Journal of Metamorphic Geology, 34*(9), 871-892.

Petrishcheva, E., & Abart, R. (2009). Exsolution by Spinodal Decomposition I: Evolution Equation for Binary Mineral Solutions with Anisotropic Interfacial Energy. *American Journal of Science, 309*(6), 431-449.

Pitzer, K. S., & Sterner, S. M. (1994). Equations of State Valid Continuously from Zero to Extreme Pressures for H2o and Co2. *Journal of Chemical Physics, 101*(4), 3111-3116.

Plümper, O., John, T., Podladchikov, Y. Y., Vrijmoed, J. C., & Scambelluri, M. (2017). Fluid escape from subduction zones controlled by channel-forming reactive porosity. *Nature Geosci, 10*(2), 150-156. Article.

Powell, R., & Holland, T. (1999). Relating formulations of the thermodynamics of mineral solid solutions: Activity modeling of pyroxenes, amphiboles, and micas. *American Mineralogist, 84*(1-2), 1-14.

Rossi, C. C. R. S., Cardozo, L., & Guirardello, R. (2009). Gibbs free energy minimization for the calculation of chemical and phase equilibrium using linear programming. *Fluid Phase Equilibria, 278*(1-2), 117-128.

Rundle, J. B., Stein, S., Donnellan, A., Turcotte, D. L., Klein, W., & Saylor, C. (2021). The complex dynamics of earthquake fault systems: new approaches to forecasting and nowcasting of earthquakes. *Reports on Progress in Physics, 84*(7).

Shao, H. B., Dmytrieva, S. V., Kolditz, O., Kulik, D. A., Pfingsten, W., & Kosakowski, G. (2009). Modeling reactive transport in non-ideal aqueous-solid solution system. *Applied Geochemistry, 24*(7), 1287-1300.

Shomate, C. H. (1954). A Method for Evaluating and Correlating Thermodynamic Data. *Journal of Physical Chemistry, 58*(4), 368-372.

Sonnenthal, E., Ito, A., Spycher, N., Yui, M., Apps, J., Sugita, Y., et al. (2005). Approaches to modeling coupled thermal, hydrological, and chemical processes in the Drift Scale Heater Test at Yucca Mountain. *International Journal of Rock Mechanics and Mining Sciences, 42*(5-6), 698-719.

Steefel, C. I. (2019). Reactive Transport at the Crossroads. *Reviews in Mineralogy and Geochemistry, 85*(1), 1-26.

Steefel, C. I., Appelo, C. A. J., Arora, B., Jacques, D., Kalbacher, T., Kolditz, O., et al. (2014). Reactive transport codes for subsurface environmental simulation. *Computational Geosciences, 19*(3), 445-478.

Steefel, C. I., DePaolo, D. J., & Lichtner, P. C. (2005). Reactive transport modeling: An essential tool and a new research approach for the Earth sciences. *Earth and Planetary Science Letters, 240*(3-4), 539-558.

Sverjensky, D. A., Harrison, B., & Azzolini, D. (2014). Water in the deep Earth: The dielectric constant and the solubilities of quartz and corundum to 60 kb and 1200 degrees C. *Geochimica Et Cosmochimica Acta, 129*, 125-145.

Tanger, J. C., & Helgeson, H. C. (1988). Calculation of the Thermodynamic and Transport-Properties of Aqueous Species at High-Pressures and Temperatures - Revised Equations of State for the Standard Partial Molal Properties of Ions and Electrolytes. *American Journal of Science, 288*(1), 19-98.

Tian, M., & Ague, J. J. (2014). The impact of porosity waves on crustal reaction progress and CO2 mass transfer. *Earth and Planetary Science Letters, 390*, 80-92.

Ulrich, T., Vater, S., Madden, E. H., Behrens, J., van Dinther, Y., van Zelst, I., et al. (2019). Coupled, Physics-Based Modeling Reveals Earthquake Displacements are Critical to the 2018 Palu, Sulawesi Tsunami. *Pure and Applied Geophysics, 176*(10), 4069-4109.

Van Laar, J. J. (1906). *Sechs Vorträge über das thermodynamische Potential und seine Anwendungen auf chemische und physikalische Gleichgewichtsprobleme : eingeleitet durch zwei Vorträge über nichtverdünnte Lösungen und über den osmotischen Druck / von J. J. van Laar*. Braunschweig: Vieweg.

Vehling, F., Hasenclever, J., & Rüpke, L. (2020). Brine Formation and Mobilization in Submarine Hydrothermal Systems: Insights from a Novel Multiphase Hydrothermal Flow Model in the System H2O–NaCl. *Transport in Porous Media, 136*(1), 65-102.

Vrijmoed, J. C., & Podladchikov, Y. Y. (2015). Thermodynamic equilibrium at heterogeneous pressure. *Contributions to Mineralogy and Petrology, 170*(1).

Wagner, W., & Pruss, A. (2002). The IAPWS formulation 1995 for the thermodynamic properties of ordinary water substance for general and scientific use. *Journal of Physical and Chemical Reference Data, 31*(2), 387-535.

Wanner, C., Peiffe, L., Sonnenthal, E., Spycher, N., Iovenitti, J., & Kennedy, B. M. (2014). Reactive transport modeling of the Dixie Valley geothermal area: Insights on flow and geothermometry. *Geothermics, 51*, 130-141.

Weis, P., Driesner, T., & Heinrich, C. A. (2012). Porphyry-Copper Ore Shells Form at Stable Pressure-Temperature Fronts Within Dynamic Fluid Plumes. *Science, 338*(6114), 1613-1616.

White, R. W., Powell, R., & Holland, T. J. B. (2007). Progress relating to calculation of partial melting equilibria for metapelites. *Journal of Metamorphic Geology, 25*(5), 511-527.

White, R. W., Powell, R., & Phillips, G. N. (2003). A mineral equilibria study of the hydrothermal alteration in mafic greenschist facies rocks at Kalgoorlie, Western Australia. *Journal of Metamorphic Geology, 21*(5), 455-468.

White, W. B., Johnson, S. M., & Dantzig, G. B. (1958). Chemical Equilibrium in Complex Mixtures. *Journal of Chemical Physics, 28*(5), 751-755.

Wilson, C. R., Spiegelman, M., van Keken, P. E., & Hacker, B. R. (2014). Fluid flow in subduction zones: The role of solid rheology and compaction pressure. *Earth and Planetary Science Letters, 401*, 261-274.

Zhang, C., & Duan, Z. H. (2009). A model for C-O-H fluid in the Earth's mantle. *Geochimica Et Cosmochimica Acta, 73*(7), 2089-2102.

Zhang, X., Ma, F., Dai, Z., Wang, J., Chen, L., Ling, H., & Soltanian, M. R. (2022). Radionuclide transport in multi-scale fractured rocks: A review. *Journal of Hazardous Materials, 424*.

Zhang, Z. G., & Duan, Z. H. (2005). Prediction of the PVT properties of water over wide range of temperatures and pressures from molecular dynamics simulation. *Physics of the Earth and Planetary Interiors, 149*(3-4), 335-354.